UNIVERSITY OF THESSALY

SCHOOL OF ENGINEERING

DEPARTMENT OF MECHANICAL ENGINEERING

Finite Element Modeling of Pipeline Structural Performance During S-Lay Offshore Installation

by

DEMETRIOS SPANOS

Submitted in partial fulfillment of the requirements for the degree of Master of Science in Mechanical Engineering at the University of Thessaly

Volos, 2025

Approved by the Committee on Final Examination:

Advisor	Dr. Spyros A. Karamanos
	Professor, Department of Mechanical Engineering, University of Thessaly
Member	Dr. Costas Papadimitriou
	Professor, Department of Mechanical Engineering, University of Thessaly
Member	Dr. Alexis Kermanidis
	Associate Professor, Department of Mechanical Engineering, University of Thessaly

Date Approved: 07/03/2025

Acknowledgements

I wish to express my gratitude to my supervisor Dr. Spyros A. Karamanos for his guidance, support, and patience. I truly appreciated his insights and working with him was a pleasure. I also extend my appreciation to the examination committee members Dr. Costas Papadimitriou and Dr. Alexis Kermanidis. I am most grateful to my family-my parents, Thomas and Annette, and my sister Despoina-for their unwavering support and being by my side through every step of this journey. I am thankful to my dearest friends, Alex, Kimon, Gianni, Niko, Alma and Antoni for all the unforgettable memories over the past years and very appreciative of Aris-Georgios Stamou, a doctoral student, and Dr. Ilias Gavriilidis, for generously and readily sharing their knowledge and assistance.

Demetrios Spanos

Finite Element Modeling of Pipeline Structural Performance During S-Lay Offshore Installation

DEMETRIOS SPANOS

Department of Mechanical Engineering, University of Thessaly

Supervisor: Spyros A. Karamanos

Professor of Numerical Methods-Finite Element Methods of Structures

Keywords: Offshore pipelines, s-lay installation, overbend, sagbend, finite elements, combined loading, bifurcation instability, limit moment, imperfections, Kyriakides' experiments.

Abstract - Offshore pipelines are subjected to complex loading conditions during their installation. In the S-lay method, critical stresses can occur in the overbend and the sagbend region. In the overbend, the pipeline experiences high axial force and bending and as it comes into contact with the stinger. In the sagbend, the pipeline is under intense external pressure and bending as it conforms to the ocean floor topography. Bending induces extensive ovalization of the tube's cross-section leading to reduced stiffness through limit point instability and on the side of axial compression, a bifurcation instability might be triggered before reaching a limit moment. External pressure accelerates ovalization, causing the governing collapse mechanism to appear earlier and tension enhances ovalization, especially if the pipe is bent over a rigid surface. Local imperfections such as ovalization and material anisotropy significantly impair the pipeline's loading capacity, especially under high external pressure. In this thesis the collapse behavior of imperfect pipes under combined loading conditions is investigated using a non-linear finite element simulation, aiming to reproduce numerical and experimental results presented by Kyriakides et al. regarding the sagbend and overbend regions. As a foundation for the study, numerical models for a tube under pure pressure, pure bending and combined bending and pressure are developed, which are continually utilized and expanded upon in subsequent analyses. The sagbend is analyzed using both a two-dimensional model, representing the cross section of a infinitely long, uniform pipe, and a three-dimensional formulation, which mimics the experimental setup. The overbend is, similarly, examined through a two dimensional model and a three-dimensional formulation, with the latter incorporating a rigid surface, enabling realistic simulation of the pipeline as it interacts with the stinger. Finally, a tube for deepwater applications is studied to outline the influence of initial wrinkling imperfections on the structural stability and the importance of material selection in thicker tubes.

Προσομοίωση Πεπερασμένων Στοιχείων της Δομικής Συμπεριφοράς Υποθαλάσσιων Αγωγών κατά τη Διαδικασία Πόντισης S-Lay

ΔΗΜΗΤΡΙΟΣ ΣΠΑΝΟΣ

Τμήμα Μηχανολόγων Μηχανικών, Πανεπιστήμιο Θεσσαλίας, 2025

Επιβλέπων Καθηγητής: Δρ. Σπυρίδων Α. Καραμάνος

Καθηγητής Υπολογιστικών Μεθόδων-Πεπερασμένων Στοιχείων των Κατασκευών

Λέξεις-κλειδιά: Υπεράκτιοι αγωγοί, s-lay εγκατάσταση, Overbend, Sagbend, πεπερασμένα στοιχεία, συνδυαστική καταπόνηση, λυγισμός, όριο κάμψης, ατέλειες, πειράματα Κυριακίδη.

Περίληψη - Οι υπεράκτιοι αγωγοί υπόκεινται σε σύνθετες καταπονήσεις κατά την εγκατάστασή τους. Στη μέθοδο S-lay, κρίσιμες τάσεις μπορεί να εμφανιστούν στις περιοχές του overbend και sagbend. Στην ανώτερη περιοχή (overbend), ο αγωγός υφίσταται υψηλή αξονική δύναμη και κάμψη καθώς έρχεται σε επαφή με τη κυρτή επιφάνεια (stinger). Στην κατώτερη περιοχή (sagbend), ο αγωγός υπόκειται σε έντονη εξωτερική πίεση και κάμψη καθώς συμμορφώνεται με την τοπογραφία του πυθμένα του ωκεανού. Η κάμψη οδηγεί σε εκτεταμένη οβαλοποίηση της διατομής που οδηγεί σε μειωμένη δυσκαμψία και μπορεί να προκαλέσει λυγισμό πριν από την επίτευξη του ορίου κάμψης. Η εξωτερική πίεση επιταχύνει την οβαλοποίηση, προκαλώντας νωρίτερα την εμφάνιση του κυρίαρχο μηχανισμού κατάρρευσης όπως και η αξονική δύναμη, ιδίως εάν ο σωλήνας κάμπτεται πάνω από μια κυρτή επιφάνεια. Τοπικές ατέλειες όπως η οβαλότητα και η ανισοτροπία υλικού μειώνουν σημαντικά την αντοχή του σωλήνα. Το φαινόμενο αυτό εντείνεται υπό υψηλή εξωτερική πίεση. Στη παρούσα εργασία η συμπεριφορά κατάρρευσης σωλήνων με ατέλειες κάτω από συνδυασμένες συνθήκες φόρτισης μελετάται αριθμητικά διαμέσου προγράμματος πεπερασμένων στοιχείων, με στόχο την αναπαραγωγή των αριθμητικών και πειραματικών αποτελεσμάτων του Κυριακίδη et al. όσον αφορά τις περιοχές sagbend και overbend. Ως βάση για τη μελέτη, αναπτύσσονται αριθμητικά μοντέλα για ένα σωλήνα υπό καθαρή πίεση, καθαρή κάμψη και συνδυασμένη κάμψη και πίεση, τα οποία αξιοποιούνται σε επόμενες αναλύσεις. Η κατώτερη περιοχή αναλύεται χρησιμοποιώντας τόσο ένα διδιάστατο μοντέλο, που αντιπροσωπεύει τη διατομή ενός απείρου μήκους, ομοιόμορφου σωλήνα, όσο και μια τριδιάστατη διαμόρφωση που μιμείται την πειραματική διάταξη. Το ανώτερο τμήμα εξετάζεται, ομοίως, μέσω ενός δισδιάστατου μοντέλου και μιας τρισδιάστατης διατύπωσης, με την τελευταία να ενσωματώνει μια άκαμπτη επιφάνεια, επιτρέποντας τη ρεαλιστική προσομοίωση του αγωγού κατά την αλληλεπίδρασή του με αυτή. Τέλος, μελετάται ένας σωλήνας για εφαρμογές βαθέων υδάτων, ώστε να παρουσιαστεί η επίδραση των αρχικών ατελειών ρυτίδωσης στη δομική σταθερότητα και η σημασία της επιλογής υλικού σε σωλήνες μεγαλύτερου πάχους.

Table of Contents

List of Figures

List of Tables

Chapter 1 – Introduction

1.1 Description of S-lay Installation Method

Offshore pipelines are vital components for transporting oil and gas from offshore wells to onshore facilities. Their design and installation present significant challenges; however, once installed, the operation of offshore pipelines typically requires a rather low maintenance cost. During the installation phase, the pipeline must withstand the applied loads with an appropriate level of safety [1], [2].

Several established methods are used to safely lay pipelines onto the seabed, including the S-lay, J-lay, Reeling, and Tow methods. The S-lay method, which is of interest to this thesis, is illustrated in **Fig. 1.1** and derives its name from the distinctive S-shaped curve the pipeline forms during installation. This method has been proposed for shallow water applications, however its use has been extended to deep waters, often where depths exceed 2,000 m. The installation process begins with the lay vessel loaded with unconnected pipe segments, transported from the coast to the site through a barge. These segments, called «line pipes», are welded together on-site on top the lay vessel, a few at a time, to form the continuous pipeline. The newly created pipeline is carefully lowered into the ocean as the vessel moves forward. At the same time, the next segments are prepared and welded to the trailing end of the pipeline. The process is repeated until the installation of the entire pipeline length is complete [1], [2].

The lay vessel is equipped with a stinger, thrusters, and a tensioner system, all of which are essential to the installation procedure. The stinger, an arm that regulates the pipeline's angle of departure, is the first point of contact for the pipeline after it departs from the vessel. It can be rigid, like a solid ramp, with constant curvature in its entire length, or articulated, comprised of many smaller sections, and its length and curvature can be adjusted to suit the laying conditions. The tensioner system provides the necessary friction through

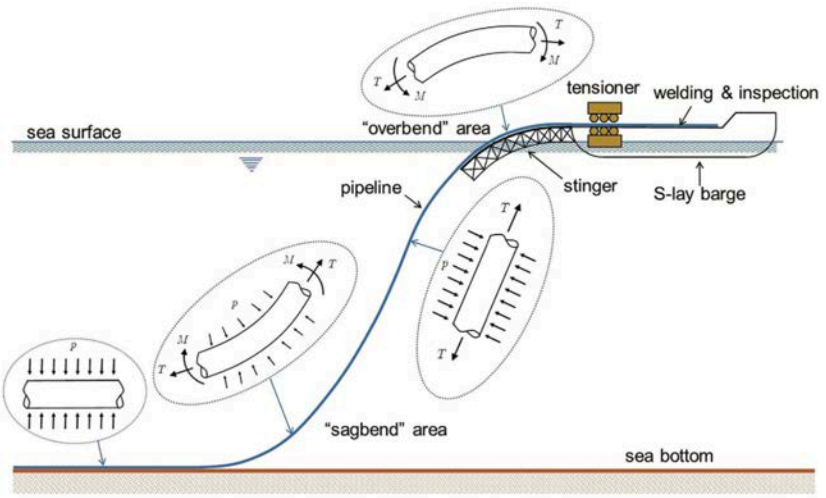

Fig. 1.1 Schematic representation of the "S-lay" pipeline installation method [2]

rubber track rollers to keep the pipeline suspended, with this force being reacted by the thruster system. Modern thruster systems are automated and make the lay operation more efficient. Throughout installation, the pipeline is typically empty with its end sealed in order to take advantage of buoyancy and reduce the required tension the vessel has to provide [1], [2], [5].

1.2 Interest of the Overbend and Sagbend Region for the Structural Integrity of the Pipeline

Internally, while in use, pipelines are subjected to high temperatures and pressures from the transported hydrocarbons, while externally they are exposed to immense hydrostatic pressure that increases proportionally with water depth. Safe operation of the pipeline mainly requires sufficient resistance to high external pressure. However, the most severe loading conditions arise during the installation phase, as the empty pipeline experiences not only external pressure, but bending and tension as well. For this reason, the installation phase represents the biggest challenge in pipeline design [1], [5].

In the S-Lay installation there are two areas of interest, where the pipeline is under combined loading, the overbend region, located at the stinger where the pipeline experiences high axial tension and bending, and the sagbend region, near the seabed, where the pipeline is subjected to intense external pressure and bending as it conforms to the ocean floor topography. The stinger, thruster and tensioner of the lay vessel must cooperate to maintain the curvature at the sagbend within acceptable bounds, and avoid local buckling.

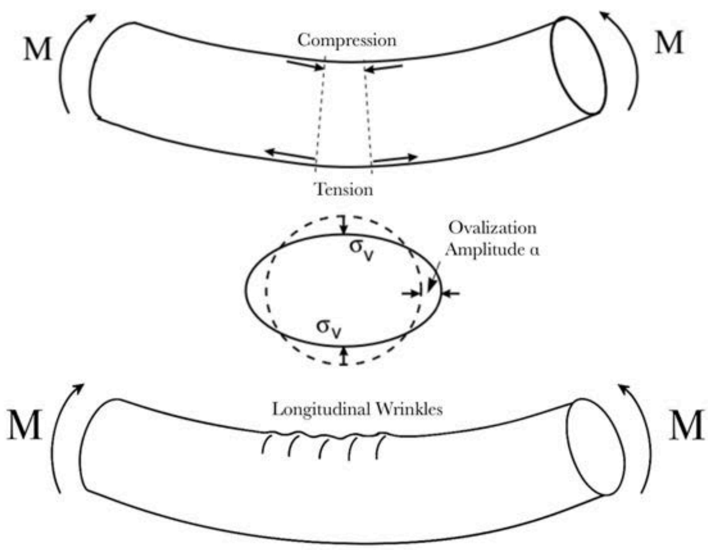

Fig. 1.2 Schematic representation of the ovalization mechanism due to the inward stress components σ_V, as well as the formation of longitudinal type wrinkles on the compression side [3]

Buckling significantly reduces pipeline stiffness and leads to local collapse, during which two opposing areas of the inner surface come into contact, forming a characteristic dog-bone shape. The goal of the operation is to avoid local buckling in both of these regions and keep the pipeline in the elastic regime, as much as that is possible [1], [5], [6].

Exposure to bending, external pressure and tension creates a challenging combination of loading conditions for the steel pipeline. A key feature of a pipe subjected to bending is the extensive ovalization of its cross-section leading to reduced stiffness through limit point instability, shown in **Fig. 1.2**. Additionally, on the side where axial compression takes place, a bifurcation instability might be triggered, marked by the formation of longitudinal wrinkles, prior to reaching a limit point. Both instabilities take place during bending, however the dominant effect is highly dependent on the tube mean-diameter-to-thickness ratio (D_m/t), with thinner tubes more prone to bifurcation instabilities. The presence of external pressure accelerates ovalization, causing the governing collapse mechanism to appear earlier. Tension can enhance ovalization by introducing stresses that promote early yielding in the material. This effect is pronounced when the pipe is bent over a rigid surface [1], [3], [6].

Naturally, the larger the depth of installation, the harsher the conditions become. For moderate to large depths, pipes of lower diameter to thickness ratios are necessary for structural stability. These thick-walled pipes buckle and collapse in the plastic region. Therefore, their material properties and imperfections play an important role in determining their final strength. In particular, imperfections such as initial ovality, wall eccentricity, material anisotropy and residual stress fields from the manufacturing technique are important to be kept to a minimum [1], [5].

1.3 Scope of the Present Thesis

The overbend and sagbend region are of primary interest in the S-Lay method. This thesis is comprised of six chapters and aims to examine the behavior of the pipeline locally in these areas and identify the circumstances necessary to ensure a safe installation. In the first chapter, a general overview of the S-Lay installation method is presented and the importance of structural stability in the critical regions is underlined. The following chapter examines the mechanics of perfect and imperfect elastic rings under pure pressure and derives the elastic buckling pressure and first yield pressure. Perfect elastic cylinders under bending are also analyzed. The third chapter focuses on the response of inelastic cylinders under pure pressure, pure bending and the combined effect of pressure and bending. Appropriate finite element models are created for each loading case with their mesh characteristics and boundary conditions specified, which set the groundwork for the following chapters. Chapter four examines the overbend region through both a two-dimensional and a three-dimensional finite element model, aiming to recreate the experiments conducted by Dyau, J. Y., & Kyriakides, S. [6] as well as their numerical formulation of a tube under tension and bending, implementing a rigid surface. The results from this work are then presented and compared. The second to last section addresses the sagbend region. Once again, a two-dimensional as well as a three-dimensional finite element model is formulated in an effort to validate the experimental data and numerical solutions of a tube subjected to combined pressure and bending performed by Kyriakides, S., Corona, E., Madhavan, R., & Babcock, C. [5]. The results are then discussed. A study of a tube suitable for deep water applications is also presented and parametrically studied through initial wrinkling imperfections when subjected to the same combined loading. The effect of material hardening in such tubes is also pointed out. The final chapter summarizes the findings.

Chapter 2 – Mechanics of Cylinders

2.1 Elastic Buckling of Perfect Rings Under Pure Pressure

This section examines the elastic buckling response of a ring subjected to external pressure. This formulation simplifies the analysis of a long, homogeneous, perfectly cylindrical shell subjected to uniform external pressure. Due to plane strain conditions, a ring (i.e., a slice of the cylindrical shell) adequately mimics the response of the shell. The wall cross-section is assumed rectangular and the applied pressure is always normal to the shell surface. The ring has a mean radius R_m and thickness t. An arbitrary point A is considered, located on the reference line, the line that passes through the centroids of all cross-sections. Its position before and after deformation are denoted by (x, y) and (x^*, y^*), respectively, and are derived from **Fig. 2.1,** where $w(\theta)$ marks the radial and $v(\theta)$ the tangential displacement. A Bernoulli type in-plane deformation is assumed, meaning every cross-section stays normal to the reference line during deformation. The following equations describe the motion of point A during elastic buckling [1], [2], [4]

$$x = R_m \cos\theta \tag{2.1}$$

$$y = R_m \sin\theta \tag{2.2}$$

$$x^* = (R_m + w)\cos\theta - v\sin\theta \tag{2.3}$$

$$y^* = (R_m + w)\sin\theta + v\cos\theta \tag{2.4}$$

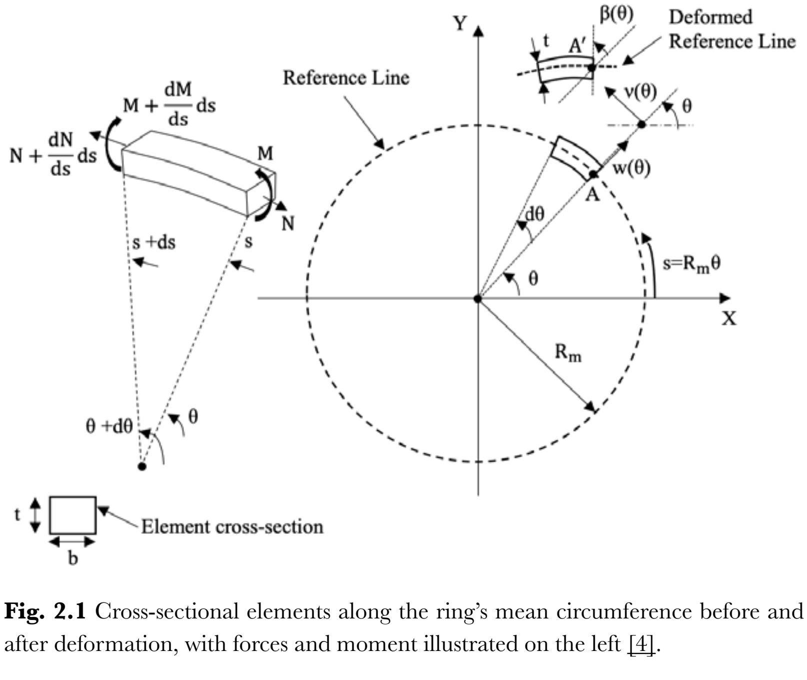

Fig. 2.1 Cross-sectional elements along the ring's mean circumference before and after deformation, with forces and moment illustrated on the left [4].

However, in thin-walled rings, deformation is assumed to be dominated by bending and effects in the axial direction can be neglected. This is the foundation of the inextensionality theory, which supports that the ring is able to change shape without altering its reference line length. Under this assumption

$$\varepsilon_m = \frac{1}{R_m}(v' + w) = 0 \Rightarrow v' = -w \tag{2.5}$$

the curvature then becomes

$$\kappa = -\frac{1}{R_m{}^2}(w'' + w) \tag{2.6}$$

A heuristic approach to derive the ring's buckling equation is by adapting the classical beam buckling equation, through the use of the so-called curvature operator. Here in ring analysis [2], [4]

$$L_\kappa(E'I\, L_\kappa(w)) - N\, L_\kappa(w) = 0 \tag{2.7}$$

where the curvature operator can be expressed as

$$L_\kappa(\cdot) = -\frac{1}{R_m^2}[(\cdot)'' + (\cdot)] \tag{2.8}$$

and

$$N = \sigma b t = \left(\frac{PD_m}{2t}\right) bt = PbR_m \tag{2.9}$$

is the axial compressive force. Substituting (2.8) and (2.9) into (2.7) the homogenous equation is derived

$$(w^{(4)} + 2w'' + w) + P^*(w'' + w) = 0 \tag{2.10}$$

where

$$P^* = \frac{PbR_m^3}{E'I} \tag{2.11}$$

is the normalized pressure. Since the ring is part of a cylinder, it has a rectangular cross section. The moment of inertia for a ring with such geometry is $I = \dfrac{bt^3}{12}$. Therefore, for a ring width $b = 1$ (i.e a thin slice of the cylinder)

$$P^* = \frac{PR_m^3}{E'\left(\frac{t^3}{12}\right)} \tag{2.12}$$

Also, under plane strain conditions, the elastic modulus is given by $E' = \dfrac{E}{1-\nu^2}$. The buckled shape of the ring can be approximated with a function of the type [1], [2]

$$w(\theta) = A\cos(n\theta) \qquad n = 1, 2, 3... \tag{2.13}$$

and substituting into the differential equation

$$[(n^4 - 2n^2 + 1) - P^*(n^2 - 1)]A\cos(n\theta) = 0 \tag{2.14}$$

Since $A\cos(n\theta)$ is the assumed solution, it has to be non-zero. This results in

$$(n^2 - 1)^2 = P^*(n^2 - 1) \qquad n = 1, 2, 3.. \tag{2.15}$$

For $n = 1$, the above equation is trivially satisfied for any value of p^*. This solution represents a rigid body translation, which is not feasible when the ring is part of a cylinder with its ends fixed. Therefore, it is not of interest and the lowest realistic eigenvalue is obtained for $n = 2$. The resulting buckling pressure is [1], [4]

$$P_{cr} = \frac{2E}{1-\nu^2}\left(\frac{t}{D_m}\right)^3 \tag{2.16}$$

and the corresponding buckling shape takes the form

$$w(\theta) = A\cos(2\theta) \tag{2.17}$$

$$v(\theta) = -\frac{A}{2}\sin(2\theta) \tag{2.18}$$

and can be seen in **Fig. 2.2**

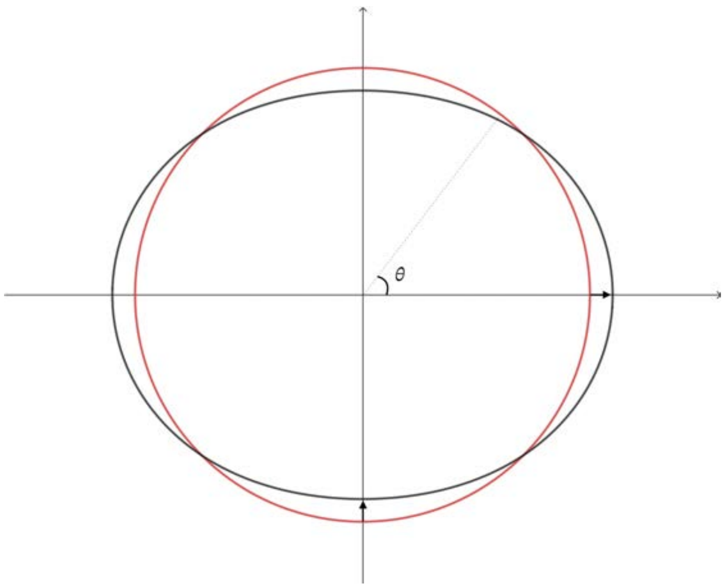

Fig. 2.2 Elastic buckling of a ring under external pressure. Red indicates the original circular shape; black shows the buckled oval form.

It is clear to see from (2.16) that the mean-diameter-to-thickness ratio (D_m/t) is the most important parameter when choosing a suitable tube for deep water installation. As mentioned before, for moderate to large depths relatively low D_m/t tubes are desirable, in the region of 15-35 [1]. In those cases, the tube collapses when the pressure reaches the yield pressure, in a phenomenon called «plastic buckling». This allows the material properties to be fully utilized. In the absence of initial imperfections or residual stresses, the yield pressure is expressed as [2]

$$P_y = 2\sigma_y \frac{t}{D_m} \tag{2.19}$$

and the critical D_m/t value that distinguishes elastic buckling from plastic buckling of a ring can be calculated as follows [2]

$$P_y \geq P_{cr} \Rightarrow 2\sigma_y \frac{t}{D_m} \geq \frac{2E}{(1-v^2)} \left(\frac{t}{D_m}\right)^3 \Rightarrow \frac{D_m}{t} \geq \sqrt{\frac{E}{(1-v^2)\,\sigma_y}} \tag{2.20}$$

Finally, the collapse pressure P_{co} ,an estimate of the maximum pressure loading a ring can withstand, is attributed to Murphey *et al.* [7] and calculated from

$$P_{co} = \frac{P_{cr}\, P_y}{\sqrt{(P_{cr}^2 + P_y^2)}} \tag{2.21}$$

2.2 Elastic Buckling of Imperfect Rings Under Pure Pressure

Imperfect rings experience elastic buckling at a lower pressure compared to their perfect counterparts and the amplitude of their initial imperfection plays a leading role in determining their strength. For convenience, it is assumed that the initial imperfection of amplitude α is in the form of the first buckling mode. The ring's initially ovalized geometry is then given by [2], [4]

$$w(\theta) = \alpha \cos(2\theta) \tag{2.22}$$

$$v(\theta) = -\frac{\alpha}{2} \sin(2\theta) \tag{2.23}$$

With the application of external pressure, the amplitude of the ovalization is expected to increase. The deformation that the ring follows has been shown to be [2], [4]

$$w(\theta) = \alpha \left(\frac{1}{1 - P/P_{cr}}\right) \cos(2\theta) \tag{2.24}$$

$$v(\theta) = -\frac{\alpha}{2}\left(\frac{1}{1 - P/P_{cr}}\right)\sin(2\theta) \tag{2.25}$$

The stress acting on the pipe wall due to pure axial compression and circumferential bending can be calculated from

$$\sigma(\theta) = \frac{N_\Theta}{t} + \left(\frac{M(\theta)}{t^2/12}\right)\frac{t}{2} \tag{2.26}$$

and the bending moment acting at each point on the circumference is given by

$$M(\theta) = \frac{3EI}{R_m^2}\left(\frac{\alpha}{1 - P/P_{cr}}\right)\cos(2\theta) \tag{2.27}$$

From equation (2.27), it is evident that the maximum bending moment, and therefore the maximum stress, is located at four equally distanced points on the reference line. For $\theta = 0, \frac{\pi}{2}, \pi, \frac{3\pi}{2}$ the stress takes the values of

$$\sigma_{max} = \frac{-PR_m}{t} \pm \left(\frac{PR_m\alpha}{1 - P/P_{cr}}\right)\frac{1}{(t^2/6)} \tag{2.28}$$

The pressure at which first yielding occurs is obtained by setting $\sigma_{max} = \sigma_y$. This leads to the following equation, attributed to Timoshenko [8]:

$$P_f^2 - \left(\frac{\sigma_y t}{R_m} + \left(1 + \frac{6R_m}{t}\left(\frac{\alpha}{R_m}\right)\right)P_{cr}\right)P_f + \frac{\sigma_y t}{R_m}P_{cr} = 0 \tag{2.29}$$

The pressure at which first yielding occurs, P_f, takes into account the initial imperfection amplitude α, the material properties and the elastic buckling pressure, which is strongly associated with the geometric characteristics of the ring. It is lower then the critical buckling pressure of the perfect elastic ring since imperfections hinder the ring's loading capabilities. The first yielding pressure is also a good ballpark estimate of the maximum loading capacity of an imperfect ring [2].

2.3 Buckling of Elastic Cylinders Under Pure Bending

This part examines the elastic buckling response of a tube subjected to pure bending. As mentioned previously, bending induces ovalization of the cross-section, eventually leading to a limit point instability, also referred to as «ovalization instability». Brazier was the first to investigate this response for long, circular, initially straight elastic tubes under pure bending, in 1927 [9]. In that work, Brazier concluded that the normalized limit moment and corresponding curvature occur when the tube's cross-section flattens by 22 % of its mean-diameter (D_m), and are equal to

$$m = 0.987 \text{ and } \kappa = 0.471 \tag{2.30}$$

where the moment and curvature are normalized respectively by

$$M_{br} = \frac{ER_m t^2}{\sqrt{1-v^2}} \text{ and } k_{br} = \frac{t}{R_m^2\sqrt{1-v^2}} \tag{2.31}$$

This behavior (induced ovalization of the cross-section) occurs in all tubes subjected to bending. In thicker tubes (low values of D_m/t) made of commonly used metals with some strain hardening, ovalization tends to localize in an area no larger than a few diameters long. In this zone, ovalization continues to grow at a fast rate as the overall moment decreases, making the limit moment the design parameter. However, thinner tubes (higher values of D_m/t) under bending are susceptible to bifurcation instabilities, referred to as «buckling» Buckling in tubes takes place under compressive loading and does not always result in yielding or fracture of the material but is still considered a failure mode, since the structure can no longer serve its intended purpose. It occurs when local stresses exceed a maximum threshold, causing the structure to bifurcate, following a new deformation path instead of the original equilibrium. For these tubes the process, as before, begins with the uniform ovalization along the length. As this ovalization localizes in an area near the mid-span, and prior to reaching a limit moment, longitudinal-type wrinkles may be observed [1], [3]. This effect typically occurs at normalized curvatures larger than 0.80. Eventually, due to the formation of these waves, the region buckles

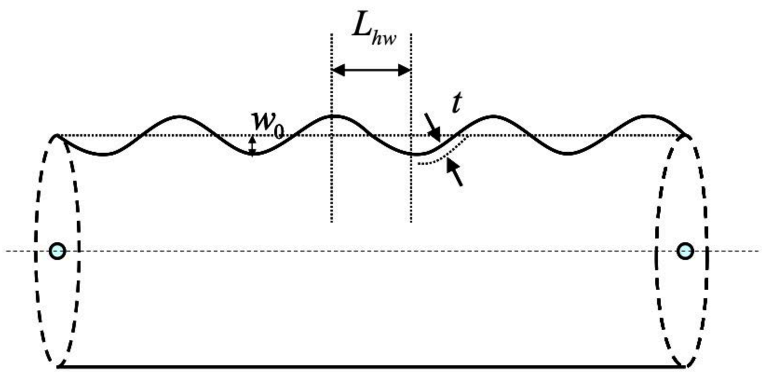

Fig. 2.3 Initial wrinkling imperfection amplitude [3]

and collapses locally, with the tube's moment reaching a maximum value before dropping sharply. In practice, outside diameter measurements are typically within 0.1% of the mean diameter value, as reported by Bardi, F., & Kyriakides, S. [13] and initial wrinkling (w_o) of about $1\% - 2.5\%$ of the tube thickness is commonly observed in pipes with D_m/t ratios in the region of $20 - 50$ which are of interest to this thesis [1].

Chapter 3 – Pipes Under Combined Pressure and Bending

3.1 Inelastic Cylinders Under Pure Pressure

This sub-chapter continues the discussion on the elastic buckling of imperfect rings (Section 2.2) and examines the inelastic response of cylinders under pure external pressure. Specifically, the collapse mechanism after the critical elastic buckling pressure is reached. As before, a ring of mean radius R_m and thickness t with elastic-plastic material is adequate. Shortly after reaching the first yield pressure, the ring stiffness gradually declines and the collapse sequence takes place. This behavior was first studied by Palmer and Martin [10] who proposed a simple model of four equally distanced plastic hinges connected by straight line segments, creating a rhombus shape, shown in **Fig. 3.1**. On these segments the uniform pressure is replaced with concentrated forces F_p. Unlike ordinary hinges, plastic hinges have a bending moment equal to the plastic moment M_p which remains constant. A quarter of the model, a right angled triangle, is shown in the figure where the normalized vertical displacement in the «Y» axis is denoted as «x». Using geometric relations, the area under the straight segments in the deformed configuration can be expressed as [2], [4]

$$A* = \frac{R_m^2\,(1-x)\,\sqrt{1+2x-x^2}}{2} \tag{3.1}$$

and calculating the change of area ΔA from the initial state to any in between is straight forward

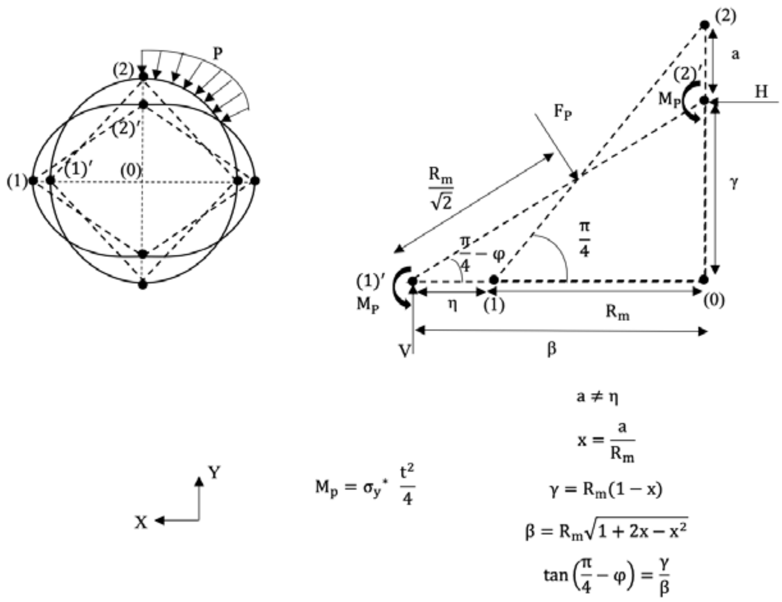

Fig. 3.1 Plastic hinge model illustrating the geometric relationships that describe cross-sectional deformation [12]

$$\Delta A = A_0 - A* = \frac{R_m^2}{2} - \frac{R_m^2 (1-x)\sqrt{1+2x-x^2}}{2} \tag{3.2}$$

The force and moment equilibrium on the deformed quarter model results in the post-buckling path of collapse under pure pressure, which relates the pressure on the outer surface with its deflection «x». This formula was derived in [4]

$$\frac{P}{P_y} = \left(\frac{t}{D_m}\right)\frac{1}{2x - x^2} \tag{3.3}$$

where

$$P_y = 2\sigma_y^* \frac{t}{D_m} \tag{3.4}$$

Yield stress, σ_y, is normally measured in uniaxial tests . However in the case of a tube, where stress is present in both the circumferential and axial direction, the Von Mises yield criterion provides a more accurate result

$$\sigma_z^2 + \sigma_\theta^2 - \sigma_z\sigma_\theta = \sigma_y^2 \tag{3.5}$$

and due to plain strain conditions

$$\varepsilon_z = \frac{1}{E}\left(\sigma_z - v\sigma_\theta\right) = 0 \Rightarrow \sigma_z = v\sigma_\theta \tag{3.6}$$

Therefore, under plane strain conditions, the hoop yield stress can be calculated as

$$\sigma_y^* = 1.125\,\sigma_y \tag{3.7}$$

Substituting (3.4) and (3.7) into (3.3) [4] [12]

$$P = 2\,\sigma_y^* \left(\frac{t}{D_m}\right)^2 \frac{1}{2x - x^2} \tag{3.8}$$

Although the collapse pressure of an imperfect elastic-inelastic ring cannot be calculated using an analytical expression, it heavily depends on the ring's initial imperfections. As mentioned above, these imperfections significantly hinder the ring's loading capabilities and are unwanted. In reality, they always exist, and have to be taken into consideration when examining a problem. Some imperfections are difficult to accurately measure and an estimate has to be taken [1]

The post-buckling response of elastic rings of perfect circular geometry was studied by Budiansky [15], and the analytical expression relating the external pressure and the ovality is presented below

$$P = P_{cr}\left(1 + \frac{27}{32}\Delta^2\right) \tag{3.9}$$

where Δ is the ovality parameter and will be explained in the following section. For the case of an imperfect elastic ring, to determine the corresponding pressure-ovality response a numerical simulation has to be conducted which follows Budiansky's analytical expression. This response is denoted as «Imperfect Elastic Response» and is shown in **Fig. 3.3**. The response of an imperfect inelastic ring follows this path until the first yield pressure, P_f, is reached. From there, it slowly starts to deviate, reaching a maximum value, P_{max}, before following the collapse path, denoted as «Plastic Mechanism».

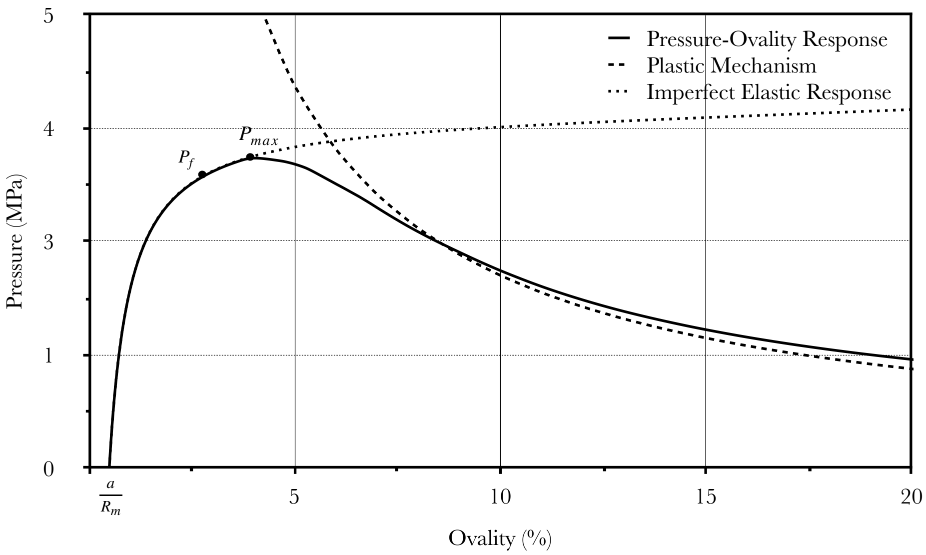

Fig. 3.2 Pressure-Ovality (%) response of an inelastic ring under pure pressure. The first yield pressure and maximum pressure are shown.

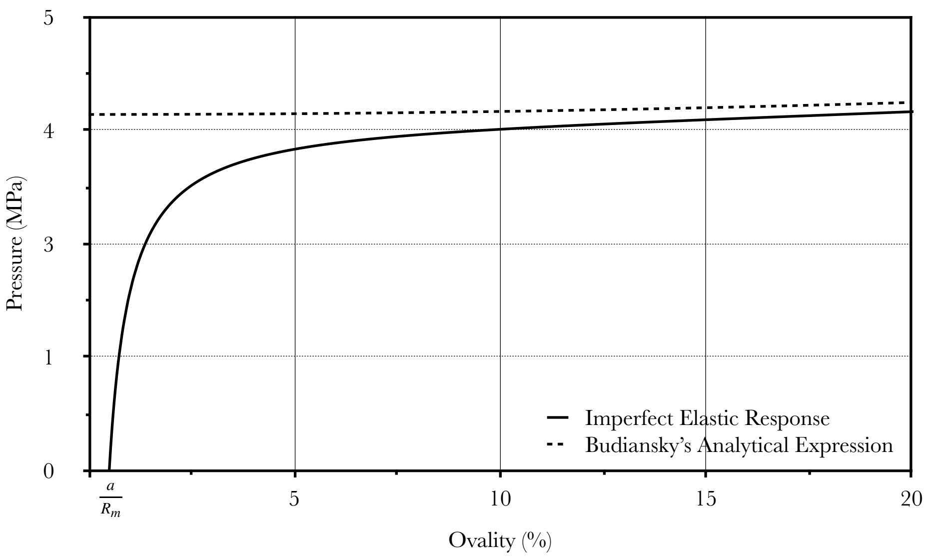

Fig. 3.3 Pressure-Ovality (%) response of an elastic ring under pure pressure. Follows the trend of Budiansky's analytical expression.

3.1.1 Initial Ovality

Initial ovality is the imperfection of interest for this thesis as it has the greatest impact to the loading ability of the ring and is commonly encountered. The term is used to express the amount the circular ring has deviated from its initially perfect shape. For a ring of mean radius R_m and thickness t, the initial geometry for an ovality amplitude of α is [1], [2]

$$w_0 = a\cos(2\theta) \tag{3.10}$$

Where α is the magnitude of the deflection of each point located at the intersection with the axes, in the initial geometry. If $R_{m,\,min}$ and $R_{m,\,max}$ are the minimum and maximum mean radius of the ring respectively, the initial ovality can be expressed as [1], [2]

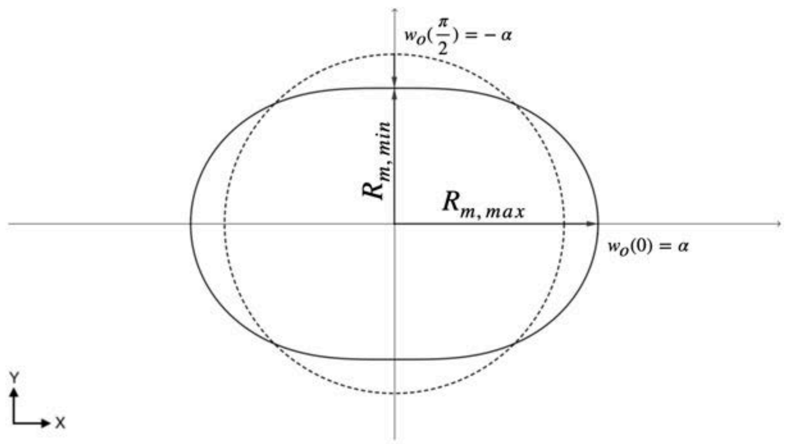

Fig. 3.4 Initially ovalized ring due to a uniform radial displacement w_o

$$\Delta_0 = \frac{R_{m,\,max} - R_{m,\,min}}{R_{m,\,max} + R_{m,\,min}} \tag{3.11}$$

This equation can be further simplified by substituting the values of $R_{m,\,min}$ and $R_{m,\,max}$. From the ring geometry [1], [2]

$$R_{m,\,\theta} = R_m + a\cos(2\theta) \tag{3.12}$$

so

$$R_{m,\,min} = R_m - a \text{ and } R_{m,\,max} = R_m + a \tag{3.13}$$

and hence,

$$\Delta_0 = \frac{R_{m,\,max} - R_{m,\,min}}{R_{m,\,max} + R_{m,\,min}} = \frac{R_m + a\ - (R_m - a)}{R_m + a\ + (R_m - a)} \Rightarrow$$

$$\Rightarrow \Delta_0 = \frac{a}{R_m} \tag{3.14}$$

3.1.2 Value Normalization

Throughout this thesis, all quantities are normalized by their respective yield values. This ensures a consistency across the results and enables direct comparison with the work of Kyriakides et al. The external pressure *P*, the bending moment *M*, and the axial tension *T*, are normalized by:

$$P_y = 2S\sigma_y \frac{t}{D_m}, M_y = \sigma_y D_m^2 t, T_y = \pi\sigma_y D_m t \tag{3.15}$$

respectively, where S is the anisotropic yield ratio that will be outlined in section 5.3. Also, the length of tube in contact with the mandrel, s, is normalized by the mandrel arc length, s_o, and ovalization is normalized by the mean minimum diameter such that $\Delta = \Delta D_{m,\min} / D_{m,\min}$. Lastly, for this work, the curvature k is measured by the end rotations of a tube under bending, according to (3.16) where «$VR1_1$» and «$VR1_2$» are the measured end rotations and «L» is the distance of the tube ends and is normalized by $k_o = t/D_m^2$. The distance «L» is considered constant, even though in reality it might slightly decrease.

$$k_{global} = \frac{VR1_1 + VR1_2}{L} \tag{3.16}$$

3.1.3 Numerical Modeling of Rings under pure pressure

A two-dimensional finite element ring model is developed in ABAQUS/Standard. This model incorporates an imperfection in the form of initial ovality of $\Delta_0 = 0.5\,\%$, as previously described, while given the double symmetry of a ring under external pressure, a quarter model is sufficient. The material used is carbon steel $X65$ and its material properties are presented in the **Table 3.1** below. With an elastic modulus of $E = 210\,\text{GPa}$, a yield stress of $\sigma_y = 449.40\,\text{MPa}$ and a poisson's ratio of $v = 0.3$, its nominal stress-strain response is illustrated in **Fig. 3.5**. In order to be inserted into the ABAQUS framework, the data pairs in the above table must be transformed into true stress - logarithmic plasticity strain. For this, the equations below are utilized

$$\sigma_T = \sigma(1+e) \text{ and } \varepsilon^{pl}{}_{ln} = \ln(1+e) - \frac{\sigma_T}{E} \tag{3.17}$$

The new data point are presented in **Table 3.2** and the material curve is given in **Fig. 3.6**

Table 3.1 Stress-Strain data pairs for $X65$ steel

Stress (σ) (MPa)	Strain (e) (%)
0.00	0.00
448.44	0.21
448.50	1.00
448.51	2.00
464.99	3.00
477.48	4.00
490.02	5.00
501.32	6.00
509.98	7.00
517.50	8.00
526.32	8.99
531.31	10.00
537.24	11.05
542.74	11.95
545.16	12.97
547.53	13.99
549.86	15.03

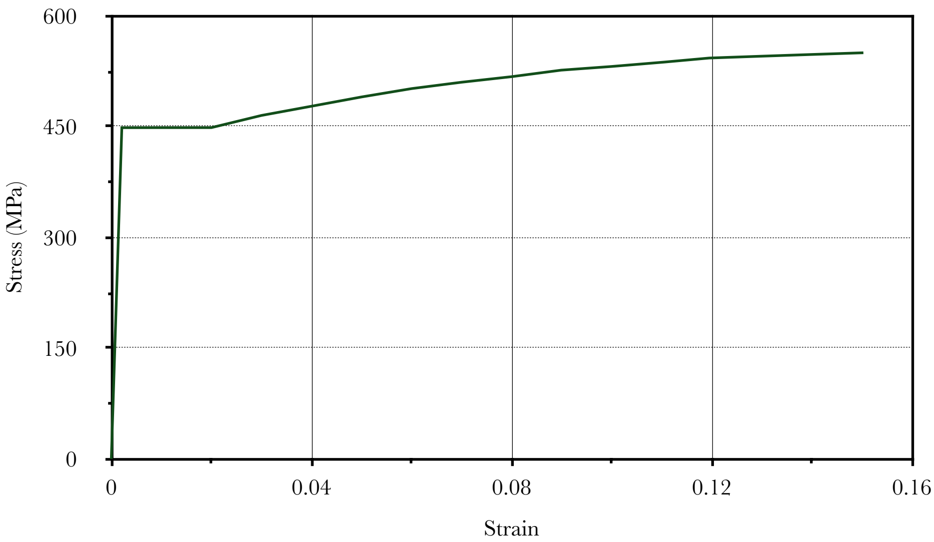

Fig. 3.5 Nominal Stress-Strain diagram for $X65$ steel

The mesh of the quarter ring consists of 50 elements in the circumferential direction and 8 elements in the through-thickness direction. The element type used is a four-node, reduced-integration, plane-strain, finite element, defined as CPE4R in ABAQUS. In **Fig. 3.7**, the model of a ring with $D_m/t = 49$ is illustrated. This D_m/t is not suitable for deepwater installations, it will serve as a general example. As mentioned, to utilize the symmetrical nature of this problem, symmetry boundary conditions have to be considered in both the top and bottom free edge of the ring. The condition of «xsymm» is applied to the top, which restricts the ring's motion in the «X» axis as well as its rotation about the «Y» and «Z» axis while «ysymm» is applied to the bottom and does not allow movement in the «Y» direction and rotation about the «X» and «Z» axis. This configuration was found sufficient to accurately predict the response of a ring under uniform pressure. In **Fig. 3.8** the boundary conditions of the ring can be seen.

Table 3.2 True Stress-Logarithmic Plastic Strain data pairs for $X65$ steel

True Stress (σ) (MPa)	Logarithmic Plastic Strain ($\varepsilon^{pl}{}_{ln}$) (%)
449.40	0.00
452.99	0.78
457.47	1.76
478.95	2.73
496.60	3.69
514.50	4.63
531.38	5.57
545.70	6.51
558.90	7.43
573.67	8.34
584.43	9.25
596.63	10.20
607.60	11.00
615.85	11.90
624.15	12.80
632.50	13.70

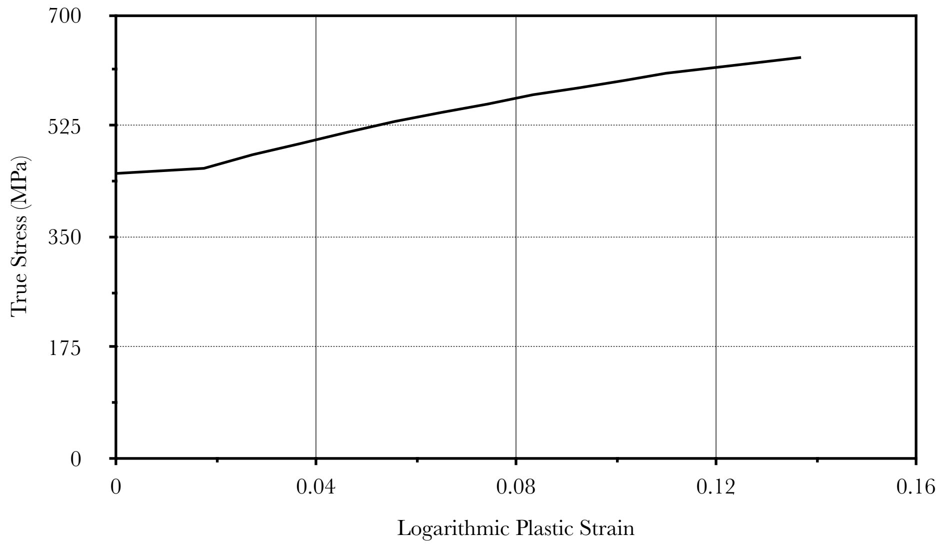

Fig. 3.6 True Stress-Logarithmic Plastic Strain diagram for $X65$ steel

The analysis described consists of two steps. In the first step, referred to as «Initial Step», the boundary conditions of the ring are applied, in the way described earlier. This also ensures rigid body motion of the ring is aborted. In the second and final step, uniform pressure is applied on the outer surface of the ring. The unstable nature of the post-buckling response of this problem requires the use of a «Riks» step. The «Riks» continuation method is very useful in snap-through buckling problems, such as this and can accurately predict the collapse pressure, the pre-buckling and unstable post-buckling response. From the response, the pressure-ovality diagram can be derived, by requesting the load proportionality factor, «LPF», which corresponds to the applied external pressure, and the displacement of a point on the minor ovalized axis, which shows the flattening of the cross section as a function of the pressure on the outer surface.

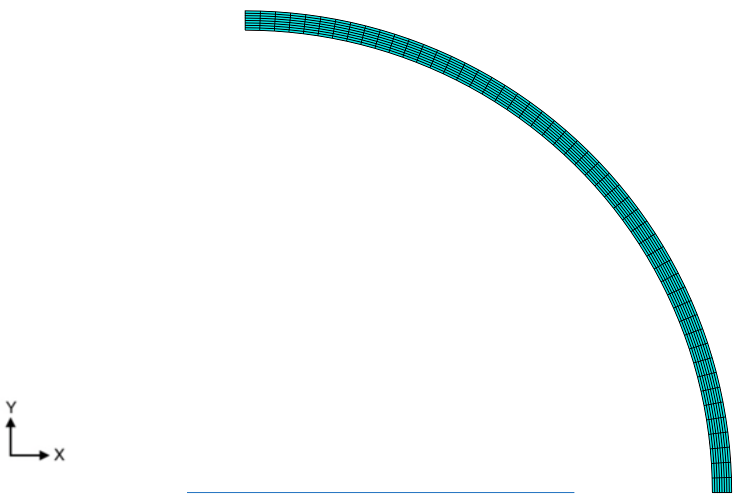

Fig. 3.7 Finite element mesh of a quarter ring composed of CPE4R elements ($D_m/t = 49$, $\Delta o = 0.5\,\%$)

To ensure the ring does not self-intersect during the collapse sequence, a two dimensional analytically rigid surface is utilized on the horizontal axis «*X*». This surface is fixed using the «Encastre» boundary condition which aborts the displacements and rotations about all the axes at a «Reference Point» assigned to it and a surface-to-surface contact constraint is created between the analytical surface and the inner surface of the ring. The penalty method is chosen as a interaction property of this contact pair.

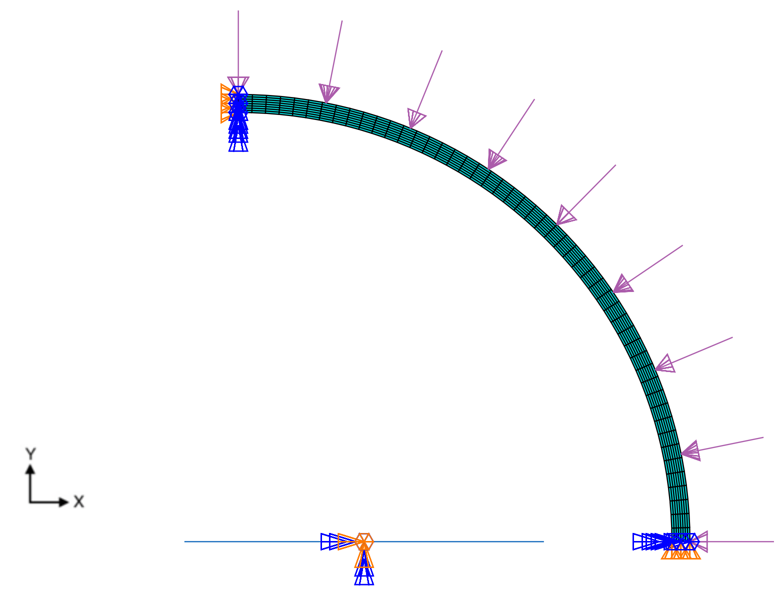

Fig. 3.8 Boundary condition configuration for a ring under pressure ($D_m/t = 49$, $\Delta o = 0.5\,\%$)

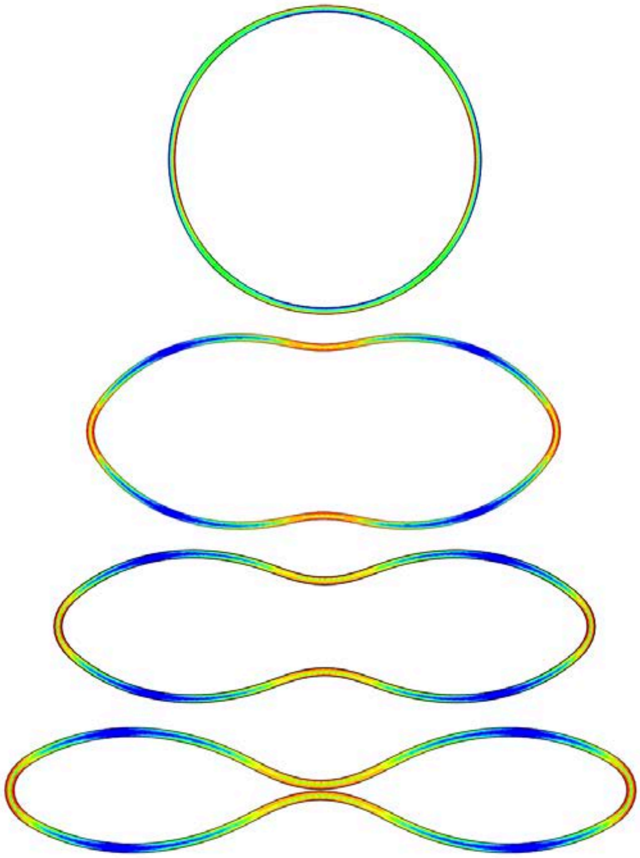

Fig. 3.9 Collapse sequence for a ring under pure pressure ($D_m/t = 49$, $\Delta o = 0.5\,\%$)

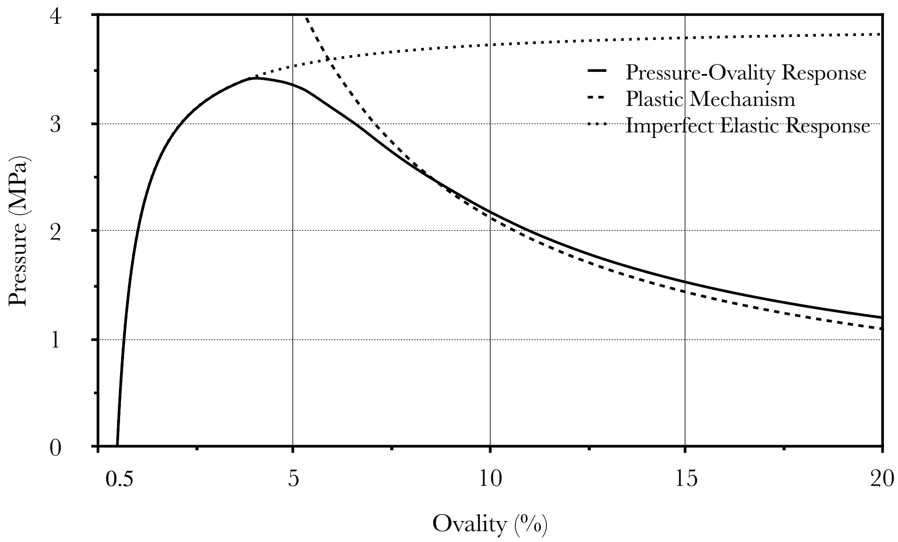

Fig. 3.10 Pressure-Ovality (%) response for a ring under pure pressure ($D_m/t = 49$, $\Delta o = 0.5\,\%$)

3.2 Elastic Rings and Cylinders Under Combined Loading

The moment-curvature response of a perfectly elastic ring is compared to Brazier's analytical expression, given in equation (3.19), in **Fig. 3.11**. It also should be mentioned that only for this section the moment and curvature is normalized by

$$M_e = \frac{ER_m t^2}{\sqrt{1-\nu^2}} \text{ and } k_N = \frac{t}{R_m^2\sqrt{1-\nu^2}} \tag{3.18}$$

While both agree well in the initial range, they diverge significantly beyond the peak moment. On the contrary, the numerical result for an elastic ring of perfect geometry under pure bending, denoted as «uniform ovalization», shows excellent agreement with the numerical formulation proposed by Karamanos, S. A. (2002) [3]. When external pressure and an initial imperfection of $\Delta o = 0.5\,\%$ is introduced, the response peaks at a lower normalized moment for a smaller normalized curvature. Increments of $10\,\%$ of the yield pressure, P_y, are applied as constant external pressure and the result is shown in **Fig. 3.12**.

$$m = \pi\kappa\left[1 - \frac{3}{2}\kappa^2\right] \tag{3.19}$$

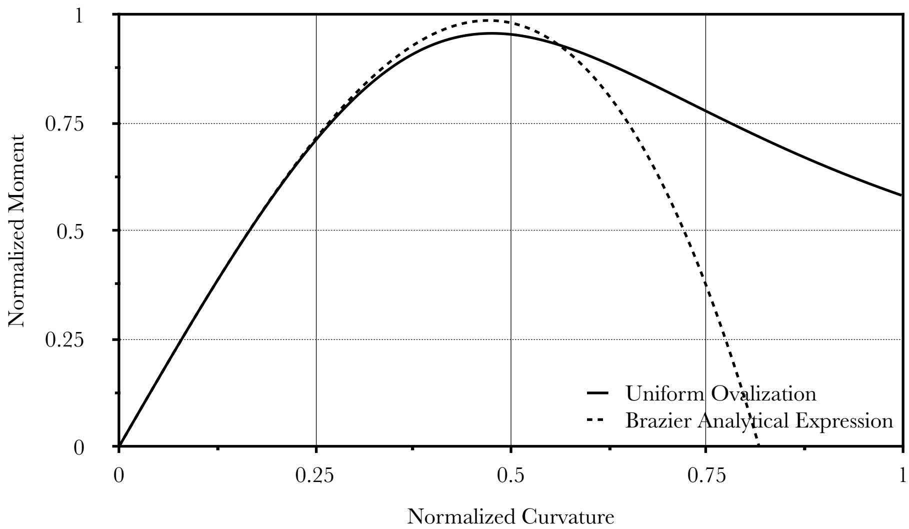

Fig. 3.11 Normalized moment–curvature response for a perfect elastic ring under pure bending ($D_m/t = 49$, $\Delta o = 0\,\%$) compared to the Brazier closed-form solution for initially straight tubes.

Lastly, when the problem is extended to an elastic tube, collapse occurs sooner due to the formation of longitudinal wrinkles on the compression side. However, up until the bifurcation point, the normalized moment-curvature response of the tube follows the uniform ovalization path. This characteristic is shown in **Fig. 3.13** for a ring and tube of $D_m/t = 49$ and $\Delta o = 0.5\,\%$.

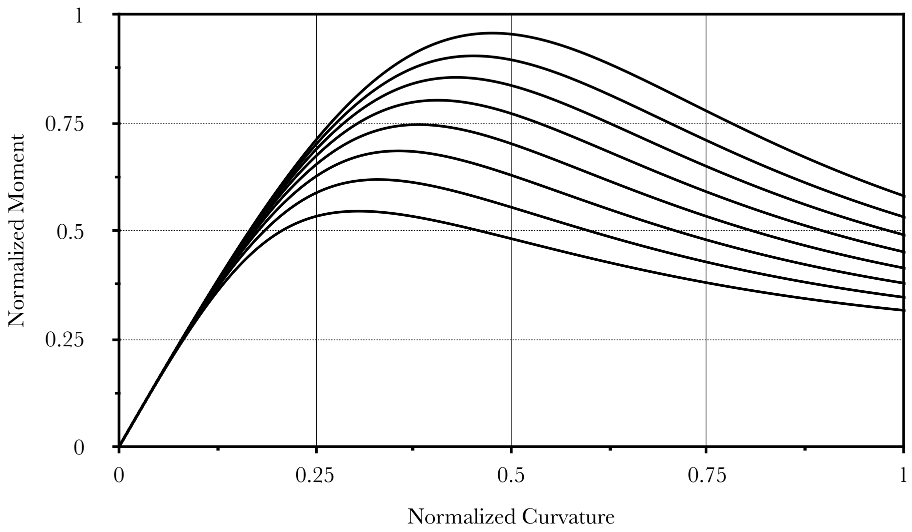

Fig. 3.12 Normalized moment–curvature responses of an elastic ring under bending, for increasing levels of constant external pressure ($D_m/t = 49$, $\Delta o = 0.5\,\%$)

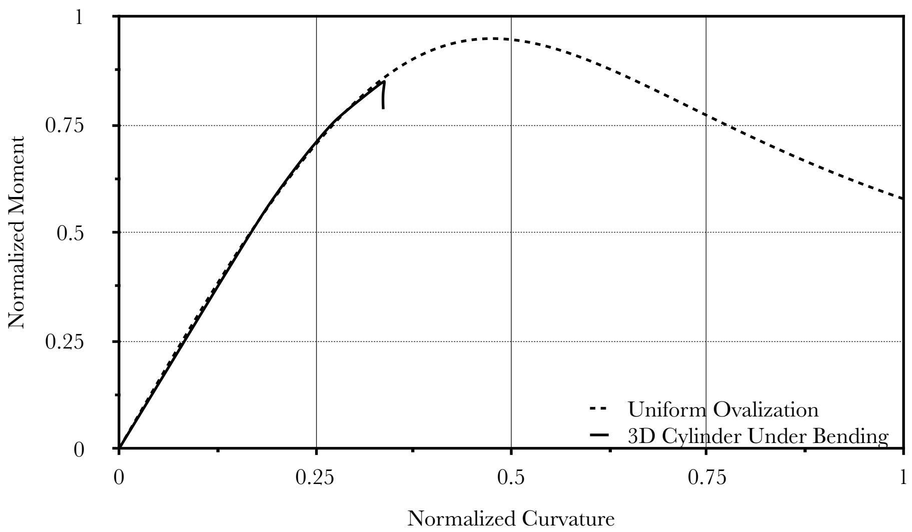

Fig. 3.13 Moment-Curvature response for an elastic cylinder under pure bending ($D_m/t = 49$, $\Delta o = 0.5\,\%$, $w_o = 1\,\%$). The response bifurcates from the path of the ring and collapses much earlier.

3.3 Inelastic Cylinders Under Pure Bending

Unlike cylinders under pure pressure, when subjected to pure bending a cylinder cannot be accurately modeled as a two-dimensional ring, as that model neglects the effects of a bifurcation instability. For this reason, the two-dimensional ring and three-dimensional cylinder model will exhibit different responses under pure bending. The curvature at which the limit moment occurs greatly varies between the two models with the former predicting a substantially higher value. However, this difference is diminished in tubes of low D_m/t value since thicker tubes are less susceptible to the effects of a bifurcation instability and extensive ovalization is the main collapse mechanism. In those cases, a two-dimensional model is sufficient to capture the response of a cylinder under pure bending [1], [2]. Both a two-dimensional and three-dimensional model will be examined in the following. The symmetrical nature of the problem can once again be taken advantage of, however, only one axis of symmetry can be utilized, as during bending one side is under tension while the other under compression.

3.3.1 Numerical Modeling of Two-Dimensional Rings Under Pure Bending

For the two-dimensional formulation, a generalized plane strain model is developed that accounts for out-of-plane axial effects. A half ring of $D_m/t = 49$, $\Delta o = 0.5\,\%$ with a mesh of 40 elements in the perimeter and 8 in the through-thickness is utilized. The material is $X65$ steel. For a tube of this D_m/t, the two-dimensional model will produce different results from the three-dimensional for the reason explained above. The element of choice is a four-node, reduced-integration, generalized plane-strain finite element, defined as CPEG4R in ABAQUS. The symmetry boundary condition «xsymm» is applied in both of the free edges. Additionally, a single node is constrained in the «Y» direction, as illustrated in the figure below, to prevent rigid body movement.

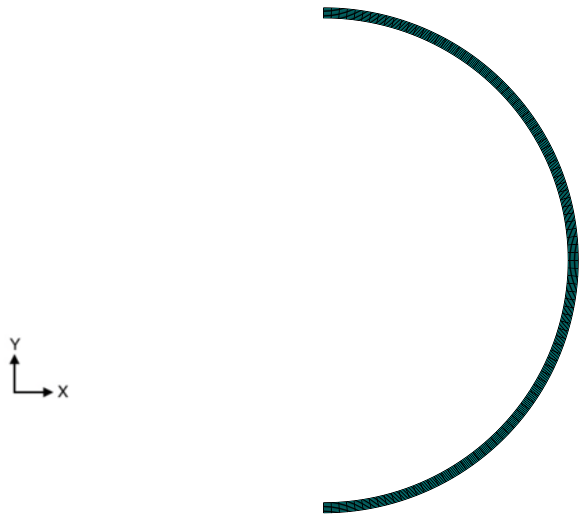

Fig. 3.14 Finite element mesh of a half ring composed of CPEG4R elements ($D_m/t = 49$, $\Delta o = 0.5\,\%$)

The analysis in question consists, once again, of two steps. In the first step, referred to as «Initial Step» in ABAQUS, the ring is adequately constrained with boundary conditions in the way described earlier. In the second and final step, a rotation is applied on the reference point of the cross section, through the input file. This displacement controlled non-linear analysis utilizes «Riks» continuation method. From the response, the moment-curvature diagram for the cross-sectional analysis of the ring can be derived, by requesting the reaction moment «RM1» and rotation «VR1» at the reference point, and is clear to see the curvature at which the limit moment is met.

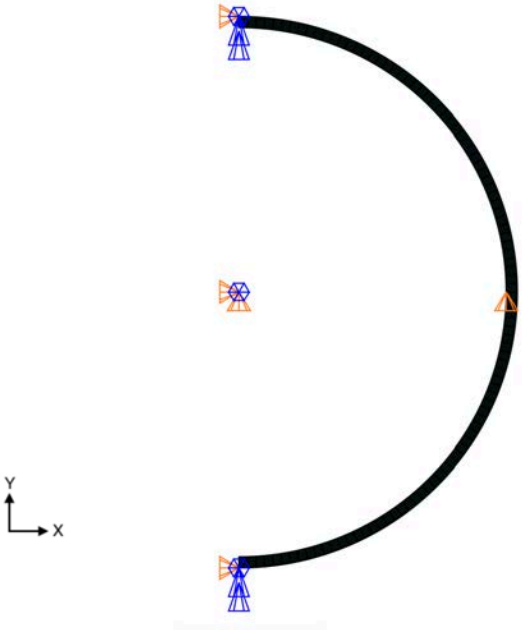

Fig. 3.15 Boundary condition configuration for a ring under bending ($D_m/t = 49$, $\Delta o = 0.5\,\%$)

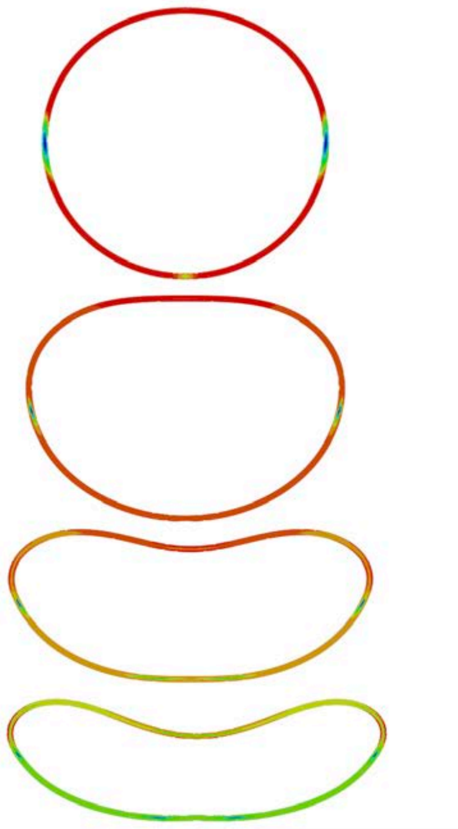

Fig. 3.16 Collapse sequence of a ring under bending ($D_m/t = 49$, $\Delta o = 0.5\,\%$)

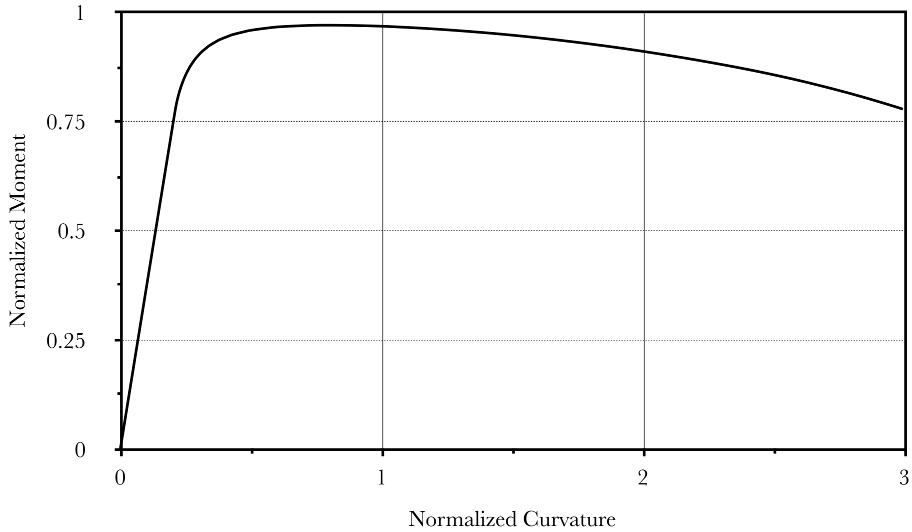

Fig. 3.17 Normalized Moment-Curvature response for a two-dimensional inelastic ring under bending ($D_m/t = 49$, $\Delta o = 0.5\,\%$)

3.3.2 Numerical Modeling of Cylinders under pure bending

The three dimensional formulation consists of a cylinder of length $L = 12D_m$, where D_m is the mean diameter of the cylinder. This length allows for the localized effects at the mid-span of the cylinder to be independent from the end conditions. A cylinder of $D_m/t = 49$, $\Delta o = 0.5\,\%$ and «$X65$» material is, once again, utilized. A mesh of 80 elements in the circumference is discretized, with 7 Gauss integration points in the through-thickness. In the axial direction, 6 elements are utilized per half-wavelength for a total of 384 elements. The element selected is a four-node, reduced-integration, shell finite element, defined as S4R in ABAQUS. Both ends of the tube are capped, meaning they are kinematically restricted in all degrees of freedom to a reference point at the centre of each end cross-section. In the «Initial Step» of the analysis, one reference point is assigned a fixed boundary condition, while the other is given a roller boundary condition, only free to move in the axial direction, and, in a subsequent step, rotations of equal magnitude but opposite direction are applied to both using an incremental scheme that follows the «Riks» algorithm. In addition to initial ovality, this model also includes an initial wrinkling imperfection of $1\,\%$ $(w/t = 0.01)$, which is measured at the highest peak of the buckling mode.

To obtain the initial wrinkling imperfection, an elastic buckling analysis of the model has to be performed. An exact copy of the model described above is created and the «Riks» step is replaced with a linear perturbation «Buckle» step, with only the first buckling mode requested. After the eigenvalue analysis is completed, an amplification factor has to be set to provide the desired initial wrinkling percentage to the initial geometry. To calculate this factor, the simplest method is to insert the mode into the «Riks» step, through the input file, with an amplification factor of unity and run the analysis. In the results visualizer, the distance between a valley and the nearest peak at the mid-span of the cylinder, where the waves have the largest amplitude, can then be measured. This distance (m) is equal to $2w$, where w is the imperfection amplitude. To achieve an initial wrinkling amplitude of 1%, the required amplification factor (a) is

$$a = \frac{2 \cdot 0.01t}{m}$$

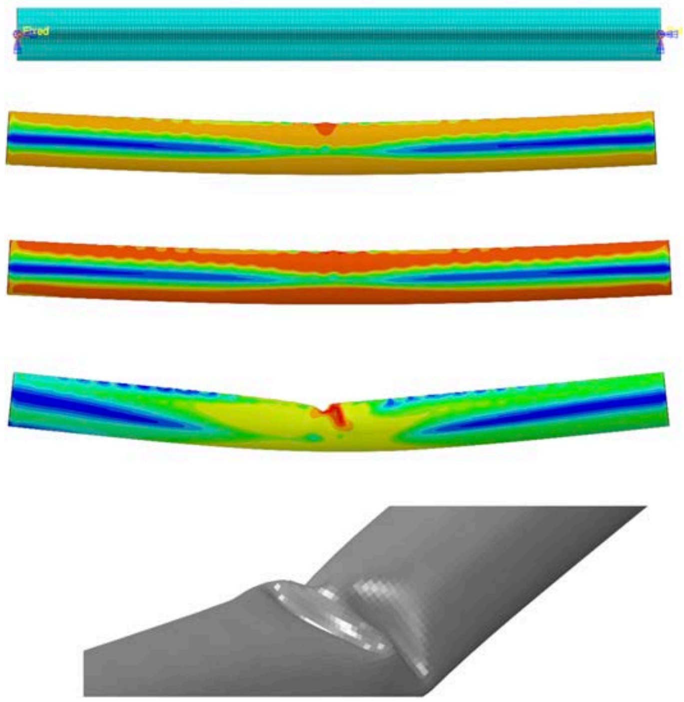

Fig. 3.18 Local buckling and collapse sequence of a cylinder under bending ($D_m/t = 49$, $\Delta o = 0.5\,\%$, $w_o = 1\,\%$)

The response of the three-dimensional model follows the ovalization path of the two-dimensional model. However, as expected, structural failure occurs much sooner due to a bifurcation instability, in the form of local buckling. The onset of wrinkling on the cylinder affects the collapse pressure, limit moment and corresponding curvature.

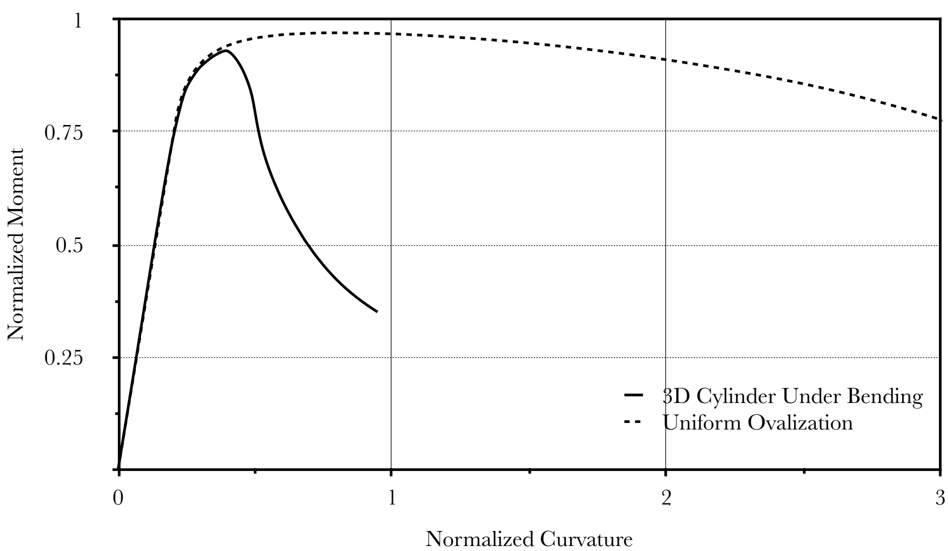

Fig. 3.19 Normalized Moment-Curvature response for a inelastic cylinder under pure bending ($D_m/t = 49$, $\Delta o = 0.5\,\%$, $w_o = 1\,\%$). The response bifurcates from the path of the ring and collapses much earlier.

3.4 Inelastic Cylinders Under Combined Bending and External Pressure

As previously mentioned, both two-dimensional and three-dimensional models can be employed, though the same exceptions mentioned in section 3.3 apply. That is, ovalization has to be the dominant collapse mechanism for the results be comparable. The modifications needed for both models are identical and only involve the addition of an extra «Static General» step. In this step, a percentage of the yielding pressure P_y, is applied to the outer surface of the cylinder in increments and kept constant during the following step, where a rotation is applied to the reference point. This loading sequence is denoted as a $P \rightarrow k$ path, and the combined loading has a severe effect on the cylinder, since external pressure magnifies the induced ovalization due to bending. Increments of $10\,\%$ of the yield pressure, P_y, are applied as constant external

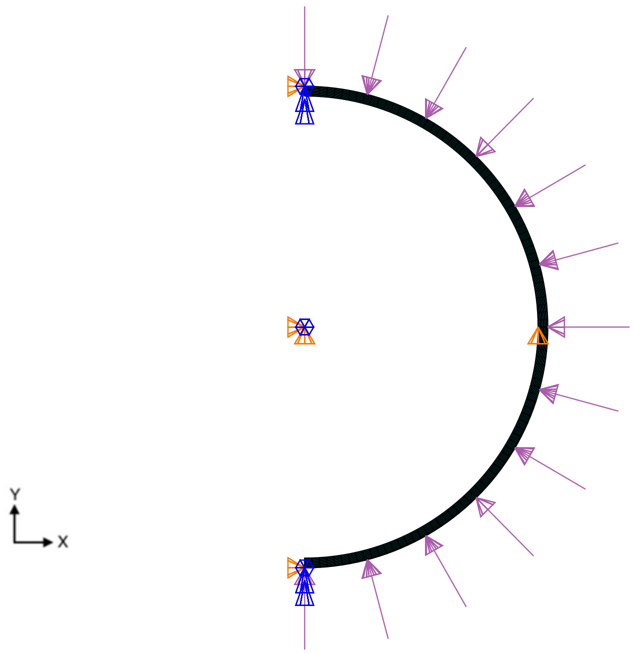

Fig. 3.20 Boundary condition configuration for a ring under combined bending and pressure ($D_m/t = 49$, $\Delta o = 0.5\,\%$)

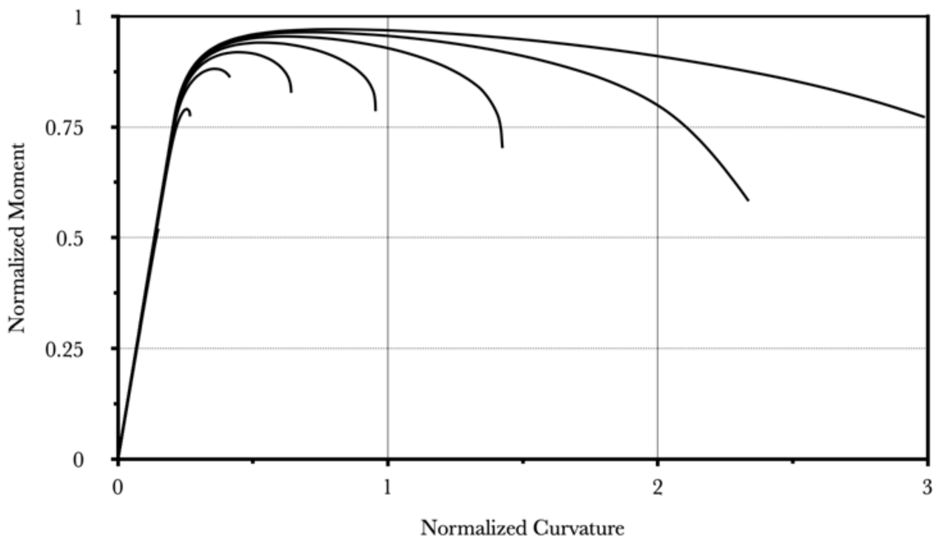

Fig. 3.21 Normalized moment–curvature responses of a ring under bending, for increasing levels of constant external pressure ($D_m/t = 49$, $\Delta o = 0.5\,\%$)

pressure. As the cylinder is bent under larger pressures its stiffness degrades faster causing the limit moment, M_o, to occur at a significantly lower curvature, k_o, compared to pure bending conditions, as seen in the graph below.

Chapter 4 – Overbend Region

4.1 Deformation Behavior and Failure Modes of Pipelines Over the Stinger

During S-Lay installation, the first point of contact for a pipeline leaving the lay vessel is the stinger. In this region, the pipeline is exposed to high tension and bending over a rigid surface. Tension results from supporting the weight of the suspended pipeline between the vessel and the seafloor, while bending is induced to the pipeline by the curved configuration of the stinger [1], [2].

The installation process is a very challenging operation, where the stinger, thruster and tensioner of the lay vessel must work together to mitigate possible threats to the structural integrity of the pipeline. The tensioner system has to precisely provide the right amount of tension to the pipeline at all times. Applying too little tension, the sagbend region is at risk of local buckling and collapse due to excessive curvature. When tension is too large, the pipeline located at the overbend is at risk of extensive ovalization and failure. As for the stinger itself, the length also has to be within reasonable bounds. A short stinger might excessively bend the pipeline due to the fast transition from the horizontal configuration of the pipe inside the vessel to the, nearly vertical, desired departure angle. Although a larger stinger might not pose dangers in the structural stability of the pipeline, it definitely increases the operation cost by adding weight and drag to the lay vessel. Therefore, the overbend region is of critical importance to the operation and the parameters must be fine tuned to avoid the mentioned failure modes [1], [2].

4.2 Description of Experiments

In this section, the experiments conducted by Dyau, J. Y., and Kyriakides, S. [6] of a tube subjected to combined bending and tension over a rigid surface will be examined. The experiment setup is comprised of a stable main support table with a vertical extension frame attached to it in the middle. On the table, there are insertions for hydraulic actuators at different intervals. In the vertical section, a rigid mandrel can also be positioned at different insertions. Tubes of length upwards of 30 times the outer diameter were used in this experiment. Their mid-span was lined up with the top point of the mandrel and the ends of the tubes attached to special end plugs. The tube ends were then attached to the free end of each of the actuators through the plugs. Both of the actuators were activated at the same time, pulling the tube ends at an angle and enforcing the tube to bend over the mandrel. The actuators were able to simultaneously apply an equal force in a quasi static manner. Appropriate sensors were also tied to them to accurately measure the force exerted. Of this force, the component perpendicular to the lift off point, which is the last point of contact between the tube and the mandrel at each moment, is denoted as «T» and is a commonly used parameter in the graphs.

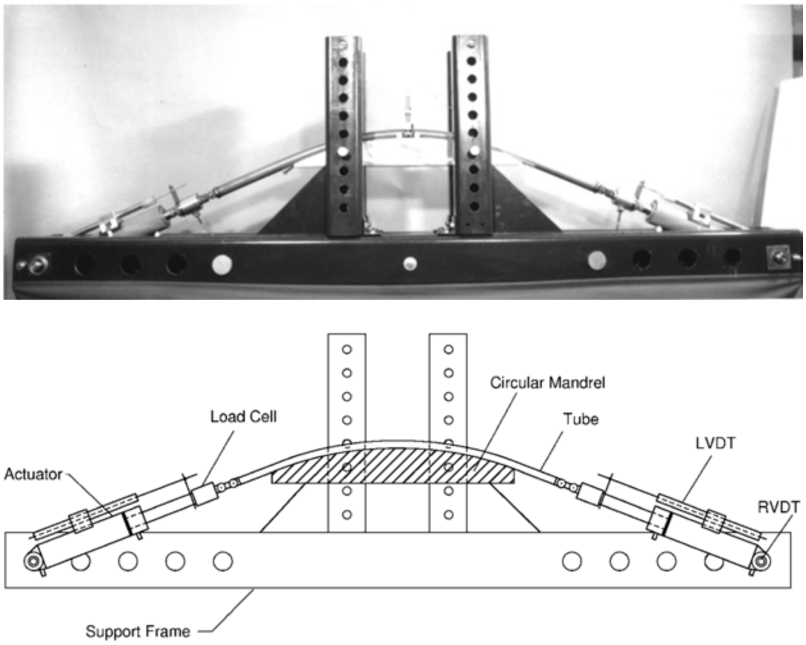

Fig. 4.1 Combined bending and tension test facility: photograph and scaled schematic [1].

During bending, a moment is created at the ends, and the force administered is reacted by the mandrel on the pipe surface. This further increases the ovalization induced by bending. To monitor the length of pipe in contact with the mandrel at any time, a special resistive paper was placed in between them and current was run through it. When a new point came into contact with a mandrel, it would register on the resistive paper. Eventually, the bottom of the pipe established contact with the mandrel at all points. From that moment on, the actuators only provided further tension to the tube. A special instrument was placed on the pipe to monitor the change in diameter of the minor axis of the ovalized tube. At specific time intervals, the actuators were paused and the instrument was rolled over the top of the bent pipe to measure the displacement of the top points, calculating the ovality at any cross section along the length.

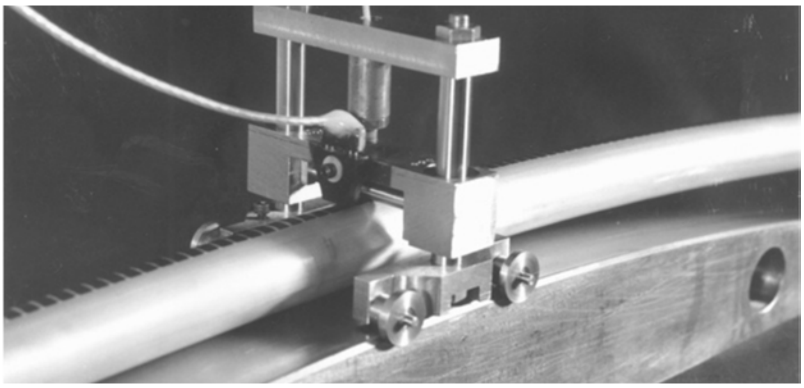

Fig. 4.2 Transducer used to scan ovalization along the length of the test specimen [1].

The configuration can be altered and the actuators and mandrel can be positioned in many ways, however, in this thesis, only the first experiment will be discussed. The pipe and configuration specifications are given in the following tables and its material is $CS1020$ [1], [6]. The following expressions apply

$$T = F \sin(\beta - \phi) \tag{4.1}$$

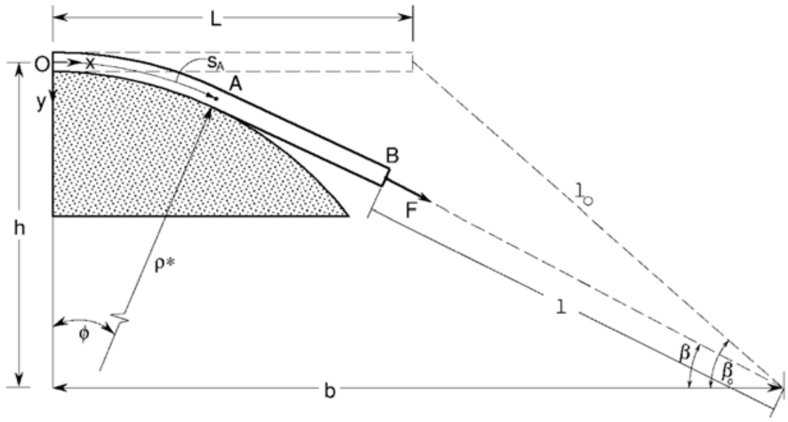

Fig. 4.3 Geometric variables of the test setup [1]

Table 4.1 Test facility configuration

Configuration			
ρ^* (mm)	b (mm)	h (mm)	s_0 (mm)
1270	1020	306	334

Table 4.2 Test specimen geometric and material parameters

Pipe							
D_m(mm)	D_m/t	L/D_m	E (GPa)	σ_y(MPa)	σ_{ro}(MPa)	n	S
30.94	34.2	32.3	212	603	572	15	1

4.3 Three-Dimensional Numerical Replication of the Experimental Procedure

An attempt is made to replicate the experimental setup, as described above. For the three-dimensional formulation of this experiment ABAQUS/Standard is used. A steel pipe of $\Delta_0 = 0.04\,\%$ with the dimensions mentioned in **Table 4.2** is created with the same mesh characteristics as in section 3.3 as they were deemed fit to give accurate results. The stress-strain curve under uniaxial behavior of $CS1020$ is approximated by a Ramberg-Osgood curve. Boasting an elastic modulus of $E = 212\,\text{GPa}$, a yield stress of $\sigma_y = 603\,\text{MPa}$, a poisson's ratio of $v = 0.3$ and coefficients of $\sigma_{ro} = 572\text{MPa}$ and $n = 15$, as measured by Dyau, J. Y., & Kyriakides, S. [6], and its nominal stress-strain and true stress-logarithmic plastic strain responses are illustrated below.

$$\epsilon = \begin{cases} \frac{\sigma}{E}, & |\sigma| \leq \sigma_y \\ \frac{\sigma}{E}\left[1 + \frac{3}{7}\left(\frac{\sigma}{\sigma_{ro}}\right)^{n-1}\right], & |\sigma| > \sigma_y \end{cases}$$

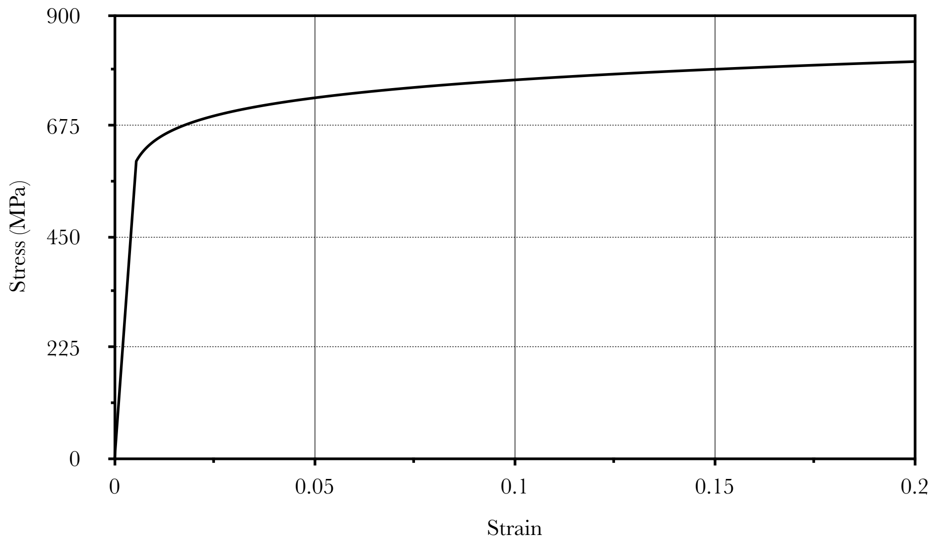

Fig. 4.4 Nominal Stress-Strain diagram for CS1020 steel

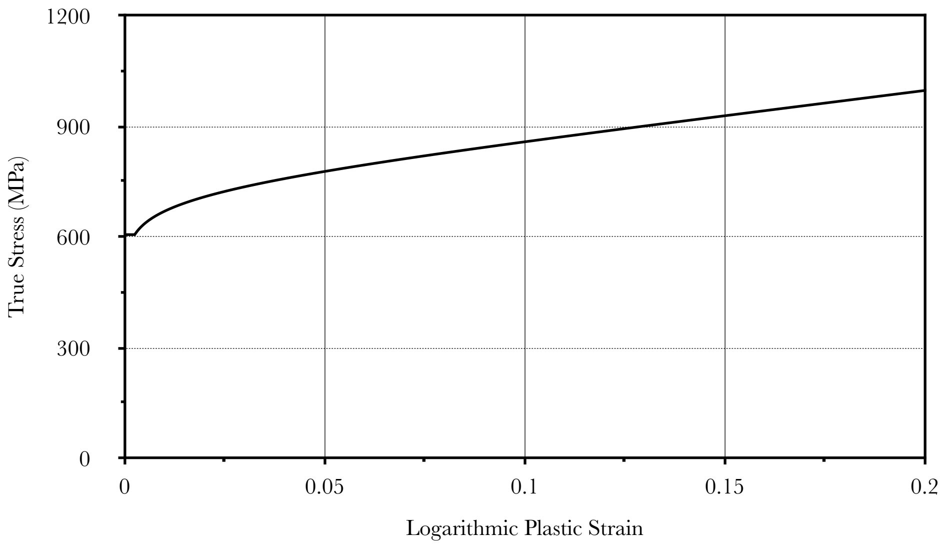

Fig. 4.5 True Stress-Logarithmic Plastic Strain diagram for CS1020 steel

The pipe is modeled as a shell by its outer diameter so that its thickness extends towards the inner side. The mandrel dimensions and the contact points of the actuators in the setup are replicated and boundary conditions are set to stabilize the tube and produce a realistic result. More specifically a condition which aborts movement in the «*Y*» axis is assigned at the node of initial contact as well as a «zsymm» condition on the mid-span cross-section. Also, a region of 36.4 mm on each end of the tube is kinematically restricted in all degrees of freedom to a reference point at the center of each end cross-section, to simulate the end plug, and a surface-to-surface interaction is created between the mandrel surface and the nodes of the cylindrical shell which are likely to come into contact with the mandrel once the tube is bent.

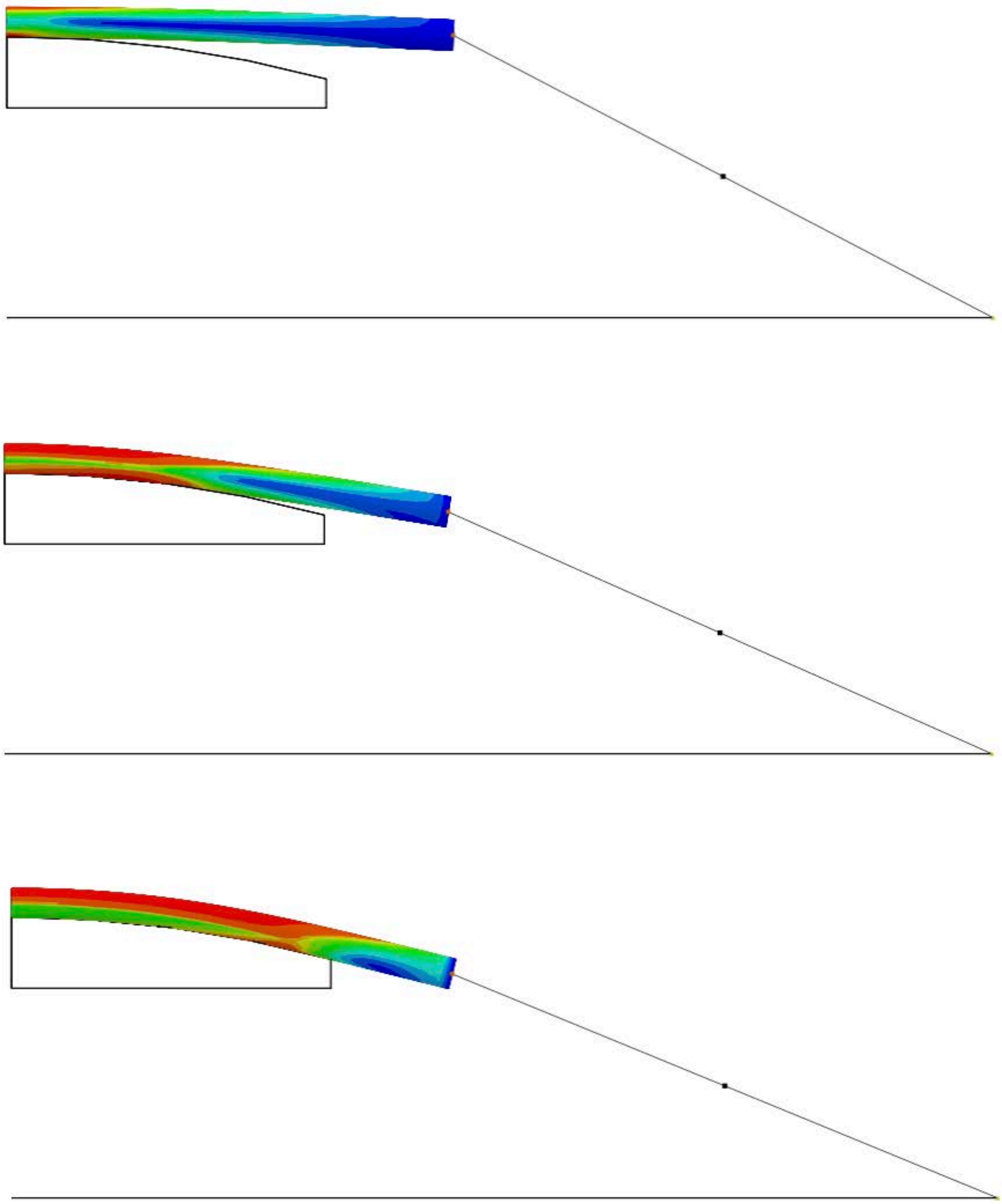

Fig. 4.6.a Numerical recreation of the combined bending and tension test facility, at different increments

To mimic the hydraulic actuators, a connector element was utilized. By assigning an axial-type connector, it is possible to connect the reference point on each end of the tube with a point on the frame. A force can then be applied to the connector in the «*X*» direction so that it utilizes its own coordinate system, not the global one, ensuring the force always points toward its fixed location on the table as the end of the tube bends and rotates. Therefore, the analysis is comprised of two steps. A «Initial Step», where the boundary conditions are applied and a loading step where the connector force is applied, in the «*X*» direction. For the actuator load history, the total force «TF» has to be selected in the field output. To calculate the tension «*T*», the location of the lift-off point has to be known at each increment to provide the angle «φ» needed in equation (4.1). The lift-off point has to be located manually through requesting a «contact pressure» plot along a path of nodes on the bottom of the pipe, for increments of interest. At any stage of deformation, when a node comes into contact with the mandrel, a peak in «Contact Pressure» occurs at the corresponding node. For this reason, measurements to calculate «T» are taken manually every few increments. For those increments, the displacement in the vertical direction of the top node of the mid-span cross-section is also measured, to calculate the ovality change, expressed as $\Delta D_{m,\min} / D_{m,\min}$, where $\Delta D_{m,\min}$ is the change in the minor mean-diameter and $D_{m,\min}$ the initial minor mean-diameter.

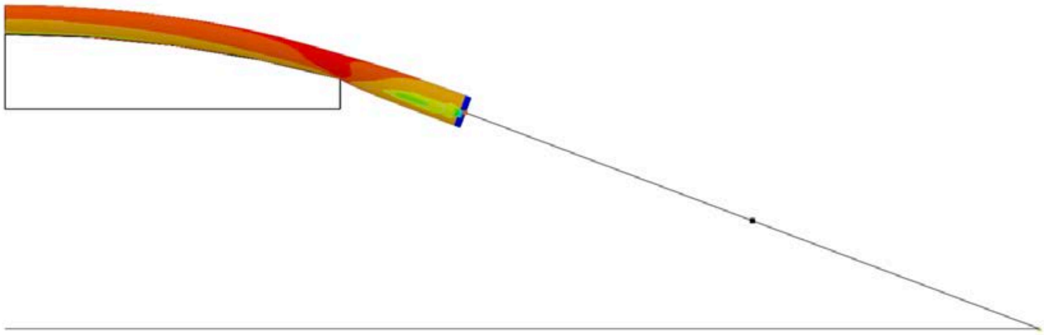

Fig. 4.6.b Numerical recreation of the combined bending and tension test facility, at different increments

The plot in **Fig. 4.7** shows the actuator force versus tube-mandrel contact length, and **Fig. 4.8** shows the ovality at mid-span versus tension. All values are normalized by their respective pair according to section 3.1.2. The results are illustrated below. In the first figure, the numerical results align well with those of Dyau, J. Y., & Kyriakides, S. [6], however they overestimate the experimental values, which is also noted by them. The predicted load is higher than the measured load. In real conditions, the problem is asymmetrical and the force from the actuators cannot be applied symmetrically at all times, leading to the variation between the left and right side of the tube, in contrast to the numerical simulation. A similar trend appears in the second figure where the predicted ovality is consistently higher than the experimentally measured value.

Despite some differences in the numerical results and the experimental data, the general trend reported in the experiments seems to be captured adequately well characterized by a peak in ovality, followed by a slight drop off and, finally, a steady rise. The maximum ovality is always associated with the lift-off point. In the beginning, this location is close to the mid-span of the tube, however it eventually moves away from it and the ovality at mid-span decreases. The convex area of the plot (for $T = 0.05T_0 - 0.1T_0$) represents the final lift-off point establishing contact with the mandrel. Its cross-section is pressed against the mandrel, providing «relief» for the rest of the pipe. Once about a quarter of the tube length is in contact with the mandrel, the ovality starts to rise again. In this configuration, the line of action of the load is purposefully, not on the tangent of the mandrel edge, meaning at full contact the force from the actuator creates a concentrated reaction on the tube from the mandrel edge. Once a large percentage of the tube is in contact with the mandrel, uniform ovalization occurs and the problem essentially becomes two-dimensional. From that point on, the actuator only provides tension and the ovality of the entire pipe gradually rises again, including the mid-span, due to the tension reaction force on its surface.

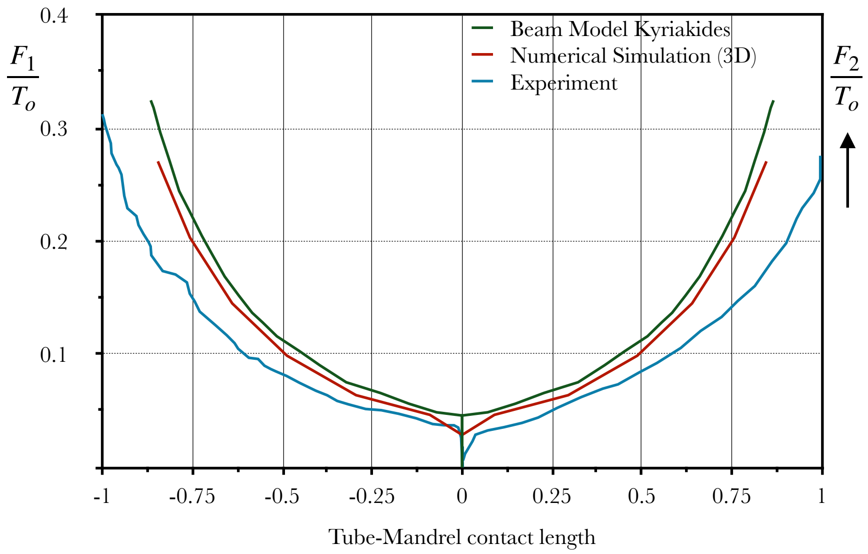

Fig. 4.7 Normalized Applied Actuator Force-Normalized Contact Length

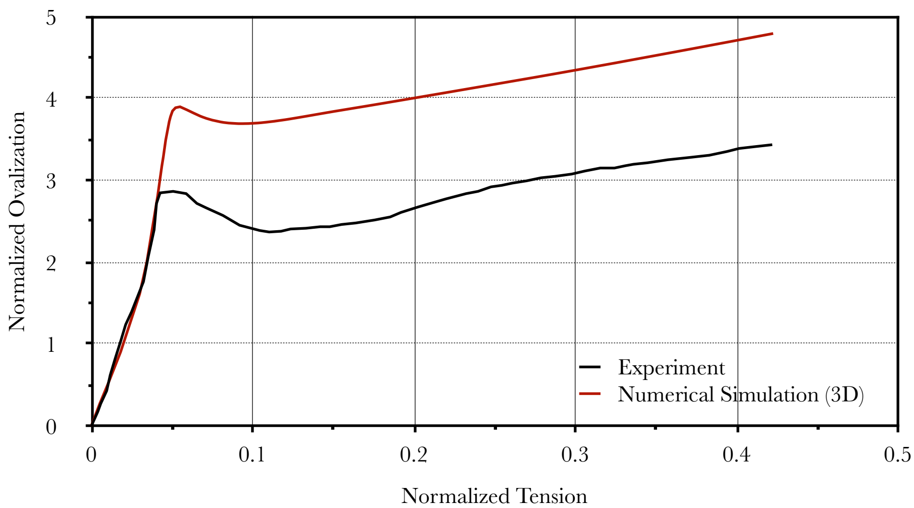

Fig. 4.8 Normalized Ovality-Normalized Tension response of the the test facility in comparison to the three dimensional numerical recreation

4.4 Two-Dimensional Numerical Simulation of Experiment

After a large part of the tube is in contact with the mandrel, the problem can be expressed in two dimensions. Therefore, a model is developed to compare the findings. The two-dimensional model follows the principles outlined in section 3.3.1. The same CS1020 steel as in the three-dimensional problem is utilized in the model. In the first step, referred to as «Initial Step» in ABAQUS, the boundary conditions of the ring are applied. The only difference to section 3.3.1 is the node constrained in the «*Y*» axis is now the lowest one to enforce ovalization towards the bottom of the ring. This boundary condition also plays the role of the rigid surface since only small ovalities are of interest, meaning only the lowest point would be in touch with the surface throughout the simulation. In the second step, which is a «Static General», the reference point is rotated to a constant angle of $0.83\kappa_o$, as mentioned in [6] and the ring is seen to ovalize. In the third and final step, an out-of- plane concentrated force is applied to the reference point as a follower force, which means it always stays perpendicular to the cross-section. Since out-of-plane forces are not allowed by default in a two-dimensional problem, a follower concentrated force is assigned in the axial direction through the input file. The vertical component of this force presses the ring against the constrained node and the resulting reaction force induces ovalization in the ring. The loading path described is a $k \to T$ (Curvature-Tension).

It is also important to mention how «T» is measured. For this loading path, since a «Riks» step is used, the «LPF» can be utilized from the history output. This loading proportionality factor is multiplied by the total force assigned for the step and results in the out-of-plane axial force, «P». However, the ring is rotated at a constant angle which means that the out-of-plane force is not perpendicular to the cross-section. Since «T» is by definition the force perpendicular to each cross-section, it has to be multiplied by «$\cos(\theta)$», where «θ» is the angle of rotation. This angle, however, is so small ~0.044° that

$$\cos(\theta) \approx 1 \tag{4.2}$$

and

$$T \approx P \tag{4.3}$$

In reality, during the experiment, the mid-span cross section is subjected to a radial loading path meaning it is incrementally prescribed tension and curvature simultaneously. This results in a modified path in the graph and a slightly higher ovalization for the ring. This path can also be recreated numerically by assigning the rotation of the reference point and the concentrated force in the same «Static General» step. The numerical results produced are illustrated below and are in excellent agreement with those of Dyau, J. Y., & Kyriakides, S. [6] Since, the «Static General» step does not produce an «LPF», an alternative was considered

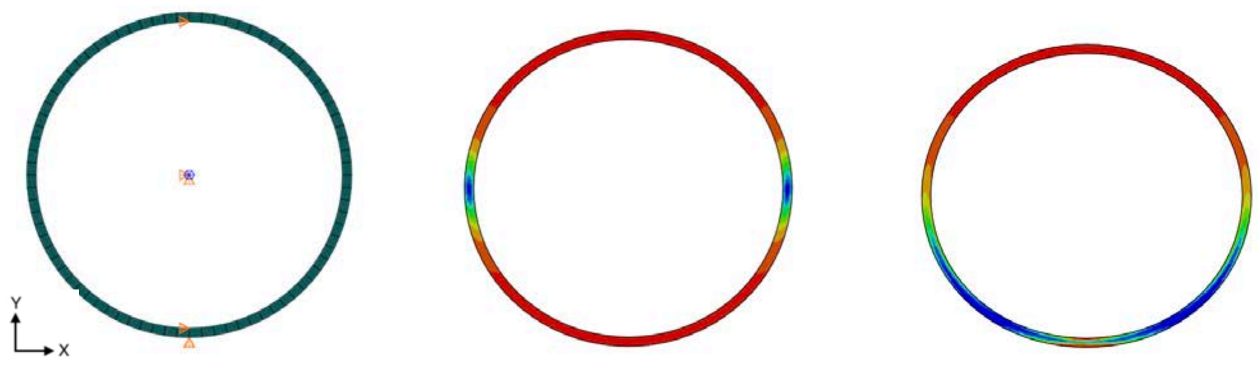

Fig. 4.9 Loading sequence of the radial path in the two-dimensional model. Initial boundary conditions, end of simultaneous rotation of the reference point and tension application, end of tension application

to calculate «T» . This consist of requesting the rotation of the reference point, «VR1» and the force component in the vertical direction «CF2». The rotation is, once again, very small and so equation (4.4) can be used. Finally, the more realistic two-dimensional radial loading path is compared to the three-dimensional experiment.

$$T \approx \frac{\mathrm{CF2}}{\tan(\theta)} \tag{4.4}$$

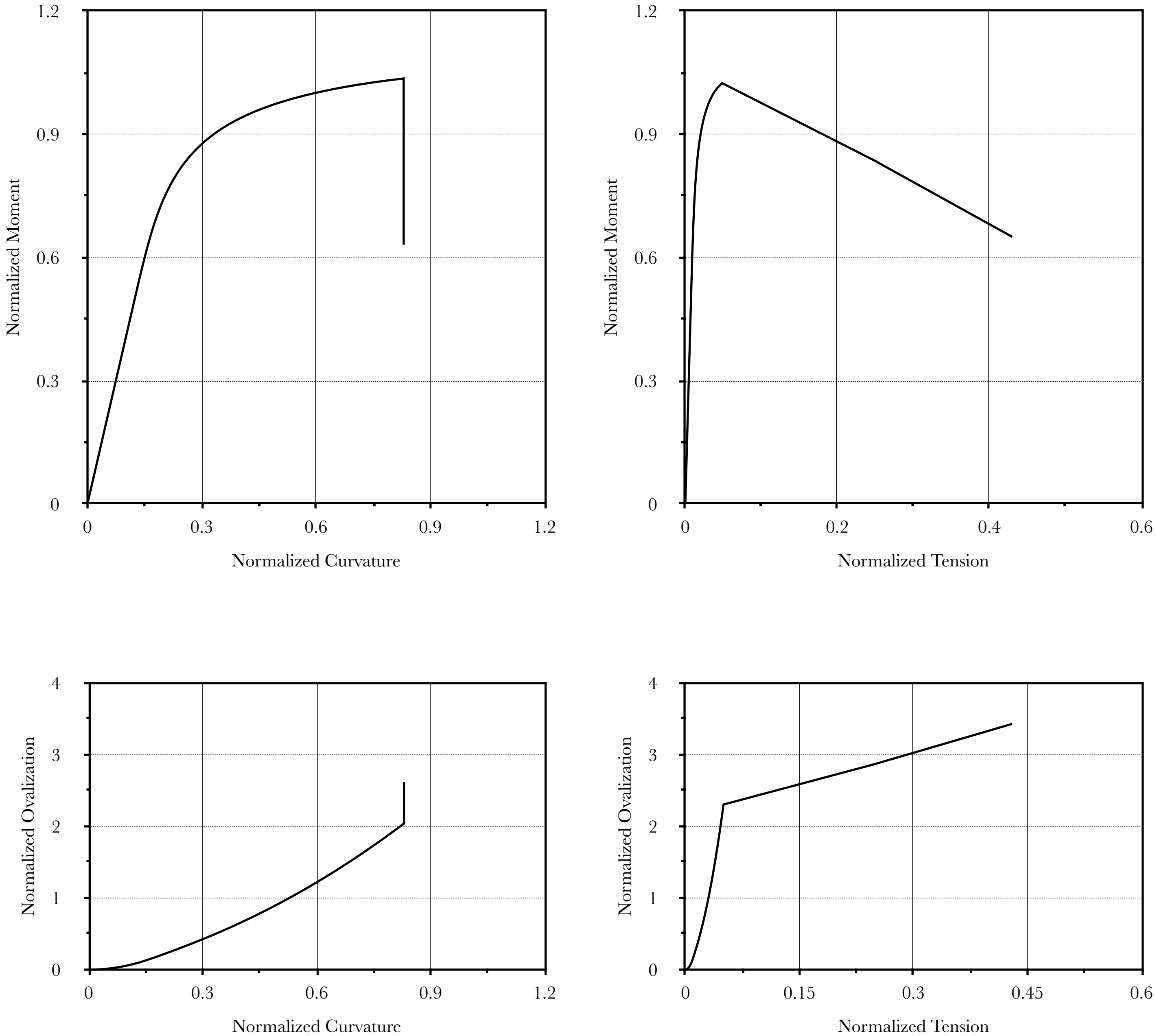

Fig. 4.10 Numerical results of radial loading path in the two-dimensional model

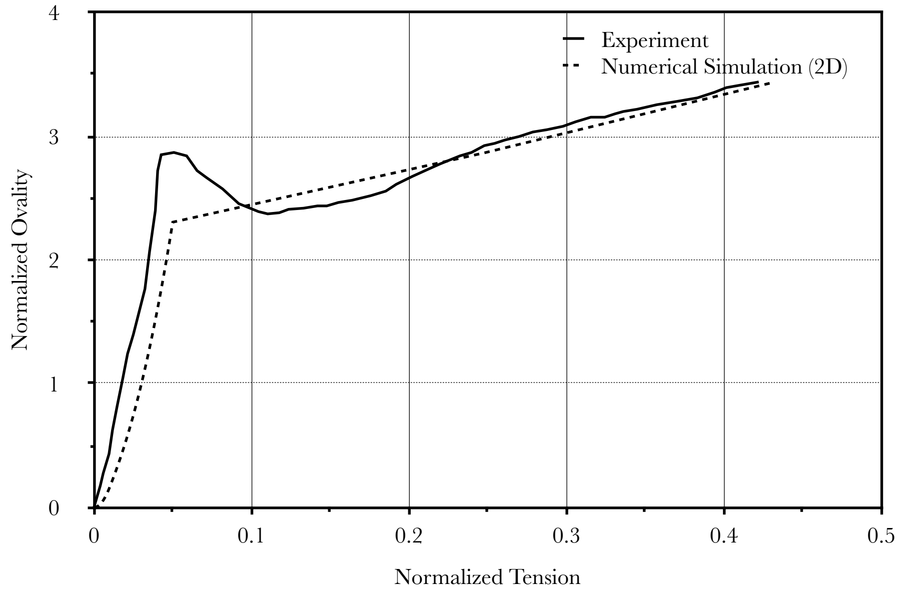

Fig. 4.11 Normalized Ovality-Normalized Tension response of the the test facility in comparison to the two dimensional numerical simulation of radial loading

Chapter 5 – Sagbend Region

5.1 Deformation Behavior and Failure Modes of Pipelines Near the Seabed

The pipeline experiences arguably the harshest loading conditions of the installation process in the sagbend region, near the seabed. In this region the pipeline is highly prone to local buckling and collapse, with structural stability primarily dependent on the parameters of the installation. Particularly, insufficient tension from the lay vessel drastically increases the risk of an accident. In this location, the pipeline is subjected to intense external pressure, due to the large water depth, and significant bending from the change in angle between the departure point and the seabed. There is also some tension present but its effects are minimal since the sagbend region is close to the seabed. During steady state laying, the pipeline behaves like a cable with its length and curvature governed by the water depth, the submerged weight and the tensioner's applied force. Once laid on the ocean-floor it is relieved of the intense combined loading conditions, providing that the seabed is relatively flat [1], [2].

5.2 Description of Experiment

This section examines the experiment conducted by Kyriakides, S., Corona, E., Madhavan, R., & Babcock, C. [5] on tubes subjected to combined bending and external pressure. The setup consists of a pure bending device enclosed into a cylindrical pressure chamber. The former features two large metal sprockets mounted on a frame at a fixed distance. For the sprockets to be able to accommodate the tube, a special mechanism is mounted which consists of four rollers, two on each side. Solid rod extensions are then fitted into the tube ends and fed through the rollers. This setup allows for axial movement of the tube ends during bending, effectively acting as a rolling contact. If a solid rod extension was not utilized, it would be difficult to measure the tube length under bending as the axial movement would lengthen the pipe segment between the sprockets. The tubes tested range from 18 to 24 diameters in length. A strong chain runs around each sprocket and each end connects to a hydraulic actuator, making for two in total. When one of the actuators contracts, the other one allows for expansion, therefore rotating the sprockets by the same amount but in opposite directions and bending the tube. It is essentially a curvature-controlled experiment. Once the tube is properly mounted on the sprockets, the device is then slid into the pressure chamber which is sealed. Prior to bending, the chamber is filled with water through a hydraulic pump in a volume-controlled fashion until the desired pressure level is reached. It is then maintained constant throughout the rest of the experiment, meaning the tube is subjected to a $P \rightarrow k$ loading path. The external pressure magnifies the induced ovalization due to bending and for large pressure levels the pipe collapse is accelerated, flattening its entire length. Once the limit moment of the tube has been reached, the actuators are stopped, the chamber is depressurized and the pipe is removed. Only the first pipe tested in the experiment will be of interest to this thesis. Its specifications and material properties are given in the following table. The material is $SS304$ [1].

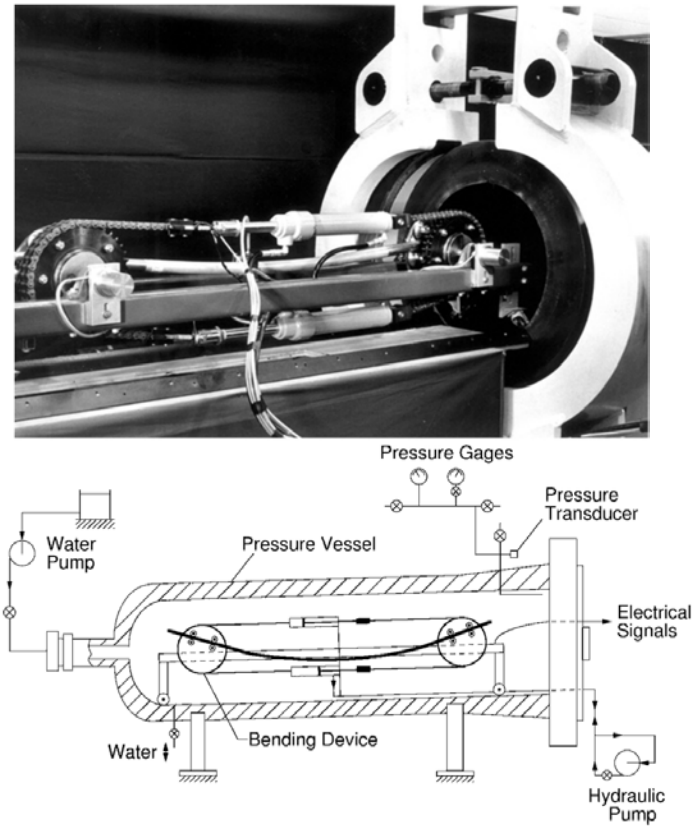

Fig. 5.1 Combined bending-pressure test facility: photograph and schematic [1]

5.3 Material Anisotropy

The fabrication and finishing process of a tube determines its final strength and properties. Tubes can be manufactured in many different ways, each with their advantages and downsides. These processes often induce material anisotropies which persist in the final product; the most common type being anisotropic yielding. As a result, tubes can experience distinct differences in their loading capabilities, commonly between the axial ($\sigma_{y,Z}$) and circumferential ($\sigma_{y,T}$) yield stress. The Hill criterion [11] can be used to examine this phenomenon and is expressed in a cylindrical coordinate system as a function

$$f = \sqrt{\sigma_Z^2 - \left(1 + \frac{1}{S_T^2} - \frac{1}{S_R^2}\right)\sigma_Z\sigma_T + \frac{1}{S_T^2}\sigma_T^2 + \frac{1}{S_{ZT}^2}\sigma_{ZT}^2} \tag{5.1}$$

where $S_T = \dfrac{\sigma_{y,T}}{\sigma_{y,Z}}$, $S_R = \dfrac{\sigma_{y,R}}{\sigma_{y,Z}}$ and $S_{ZT} = \dfrac{\sigma_{y,ZT}}{\sigma_{y,Z}}$ express the variation between the yield stress in two directions. The yield stress in the transverse, radial and longitudinal directions are marked by $\sigma_{y,T}$, $\sigma_{y,R}$ and $\sigma_{y,Z}$ respectively and under pure shear loading the yield stress is denoted by $\sigma_{y,ZT}$. When any of the S parameters take the value of unity no anisotropic yielding is present in that direction, in relation to the axial. In this thesis, it is assumed that material properties are equivalent in the transverse and radial direction and only differ in the axial. Therefore $S = S_T$, and Hill's potential function can be further simplified

$$f = \sqrt{\sigma_Z^2 - \sigma_Z\sigma_T + \frac{1}{S^2}\sigma_T^2} \tag{5.2}$$

However, to be inserted in the ABAQUS/Standard numerical framework, special R values have to be formulated instead as

$$R_{ij} = \frac{\sigma_{i,j}}{\sigma_y} \tag{5.3}$$

with $\sigma_{i,j}$ being the measured yield stress in that direction as compared to the user defined σ_y. It is possible to assign these values through the «Potential» subcategory in the material properties. Utilizing the default cylindrical coordinate system in ABAQUS, the R_{11} value is of interest. This parameter expresses the ratio of the circumferential ($\sigma_{y,T}$) to the axial ($\sigma_{y,Z}$) yield stress and allows for direct comparison to the work of Kyriakides. When material anisotropy is considered in this context, it is insinuated that only R_{11} is active and all other R parameters are set to unity, effectively treating those directions as isotropic.

5.4 Three-Dimensional Numerical Simulation of Experiments

This study aims to replicate the experimental procedure numerically using ABAQUS/Standard. Since the exact length of each tube in the experiment is not specified, a mean value of $L = 21D_m$ is assumed for the three-dimensional formulation. The pipe properties are mentioned in **Table 5.1**, with the material approximated by a Ramberg-Osgood curve. Featuring an elastic modulus of $E = 186\,\text{GPa}$, a yield stress of $\sigma_y = 259\,\text{MPa}$, a poisson's ratio of $v = 0.3$ and coefficients of $\sigma_{ro} = 224\text{MPa}$ and $n = 9.67$, as measured by Kyriakides, S., Corona, E., Madhavan, R., & Babcock, C. [5], the stainless steel's stress-strain response is illustrated in **Fig 5.2**. The data pairs must, once again, be transformed to true stress-logarithmic plastic strain pairs to be recognized by ABAQUS, shown in **Fig. 5.3**

Table 5.1 Test specimen geometric and material parameters

Pipe							
D_m(mm)	D_m/t	Δ_0(%)	E (GPa)	σ_y(MPa)	σ_{ro}(MPa)	n	S
30.79	33.94	0.04	186	259	224	9.7	0.94

The model employs the same mesh characteristics outlined in section 3.3.2. The material is also adjusted for a yield anisotropy. The tube is modeled as a shell defining its outer diameter with its thickness extending toward the inner side. Both ends of the tube are kinematically restricted in all degrees of freedom to a reference point at the center of each end cross-section. Specifically, a length of 36.4 mm on each end is constrained to simulate the length of the extension rod inserted in the experimental set up. Lastly, one reference point is fixed while the other is only allowed to move in the axial direction.

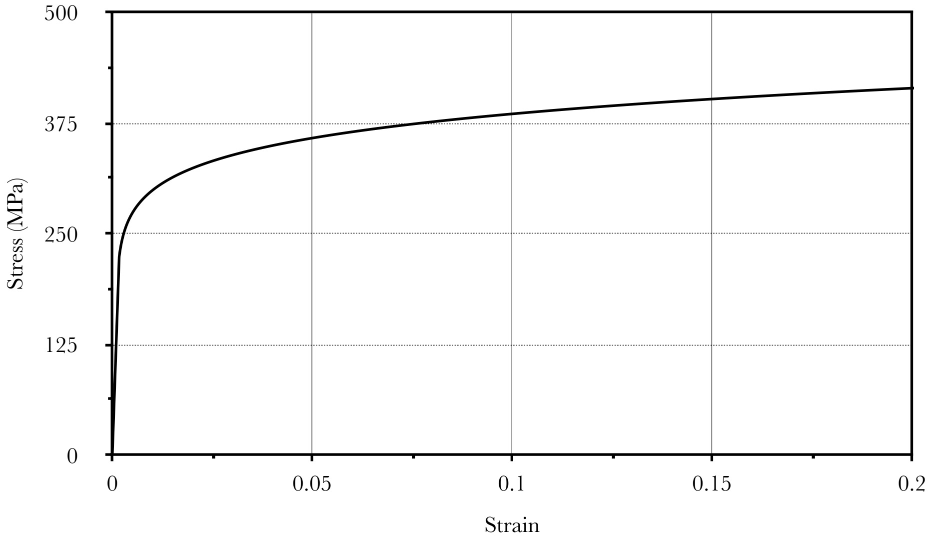

Fig. 5.2 Nominal Stress-Strain diagram for *SS* 304 steel

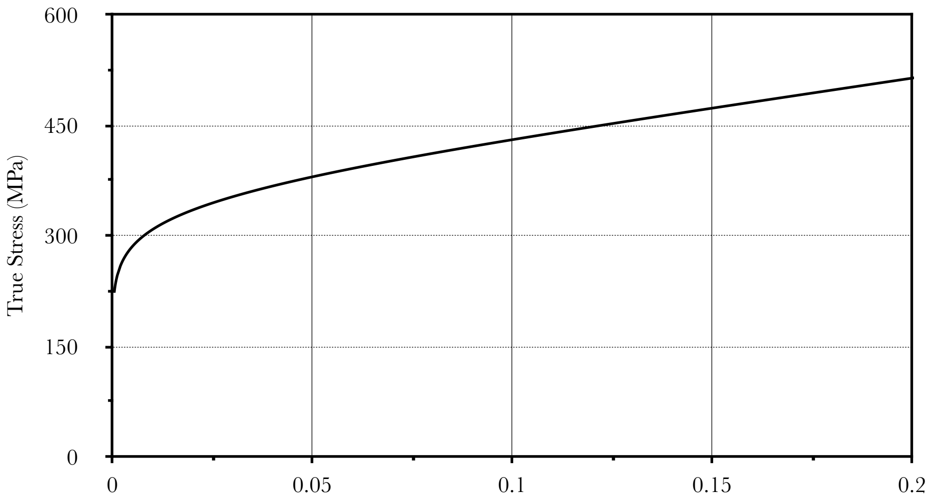

Fig. 5.3 True Stress-Logarithmic Plastic Strain diagram for *SS* 304 steel

The reason for using solid rod extensions in the experiment was explained above. In the numerical formulation, however, they are unnecessary since a rotation can be applied directly to each end, not affected by its axial movement. Therefore, each reference point is simply assigned a rotation in the opposite direction of the other making it a displacement-controlled problem. The analysis described consists of two steps. In the first step, referred to as «Initial Step» in ABAQUS, the boundary conditions of the tube are applied, in the way described earlier. In the second step, a specific level of uniform pressure, which is a percentage of the yield pressure P_y, is assigned on the outer surface of the tube through a «Static General» step. The effect of this pressure on the tube ends is also included through an axial compressive follower force on the reference point of the roller end. This force is equal to the cross-sectional area of the tube multiplied by the outer pressure. The third and final step utilizes «Riks» continuation method to apply an equal in value but opposite in direction rotation on the reference points. From the response, the m-κ (normalized moment- normalized curvature) diagram can be derived by requesting the reaction moments «RM1» and the rotations «VR1» at the reference points. The results show the curvature at which the limit moment is met for any constant external pressure.

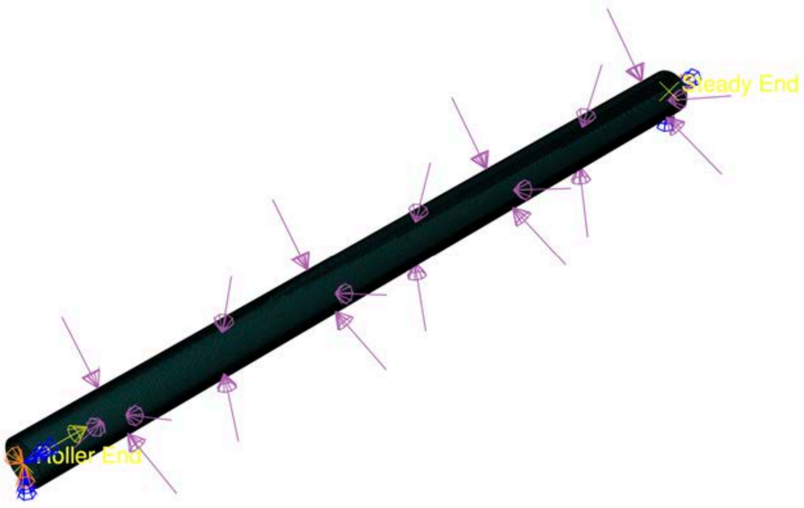

Fig. 5.4 Boundary condition configuration for a cylinder under pressure and bending ($D_m/t = 33.94$, $\Delta o = 0.04\,\%$)

This analysis is repeated for increasing values of external pressure and a curvature-pressure point is defined from the results of each analysis. The point on the horizontal axis is given by a pure bending simulation as outlined in section 3.3 while the vertical axis point by a pure external pressure simulation as seen in section 3.1.3. For all points in between, increments of $5\,\%$ of the yield pressure, P_y, are applied as constant external pressure. These points are then placed on a graph along side the experimental results. The numerical results extracted from the above model seem to reproduce the general trend of the experimental data adequately well, although on the conservative side.

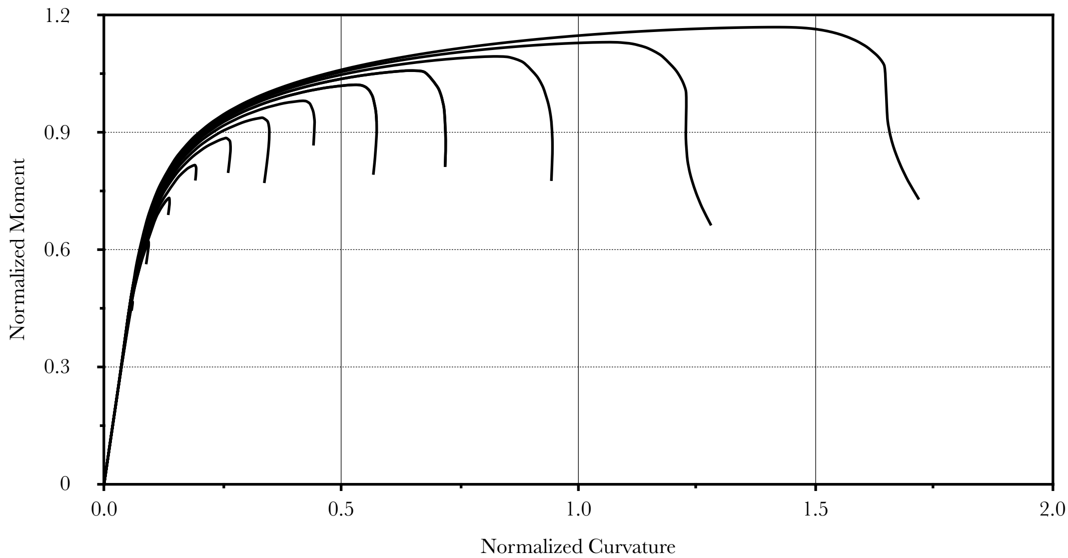

Fig. 5.5 Normalized moment–curvature responses of a cylinder under bending, for increasing levels of constant external pressure ($D_m/t = 33.94$, $\Delta o = 0.04\,\%$)

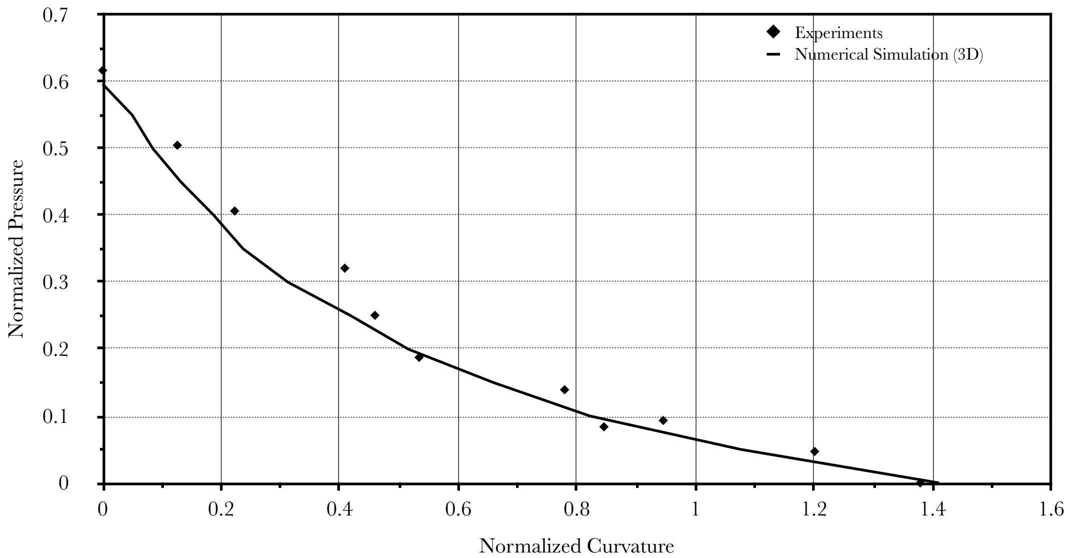

Fig. 5.6 Normalized pressure–curvature pairs of a cylinder under bending, for increasing levels of constant external pressure in comparison with Kyriakides' experimental data ($D_m/t = 33.94$, $\Delta o = 0.04\,\%$)

5.4 Two-Dimensional Numerical Simulation of Experiments

Pipes with moderately low D_m/t ratios subjected to combined pressure and bending, can be accurately approximated as two-dimensional, with the most noticeable differences between two and three-dimensional models appearing in pure bending and low-pressure cases. As the external pressure rises, the results from 2D and 3D analyses tend to converge. However, they do not always coincide because of the wrinkling effect of a three-dimensional tube that cannot be implemented into a two-dimensional model. In this case, for a $D_m/t = 33.94$ which is moderately low, a two-dimensional model may provide satisfactory results and is formulated according to section 3.4. As for the material, the same $SS304$ steel is utilized. A $P \rightarrow k$ loading path is followed and the numerical results appear to be in agreement with those of Kyriakides, S., Corona,

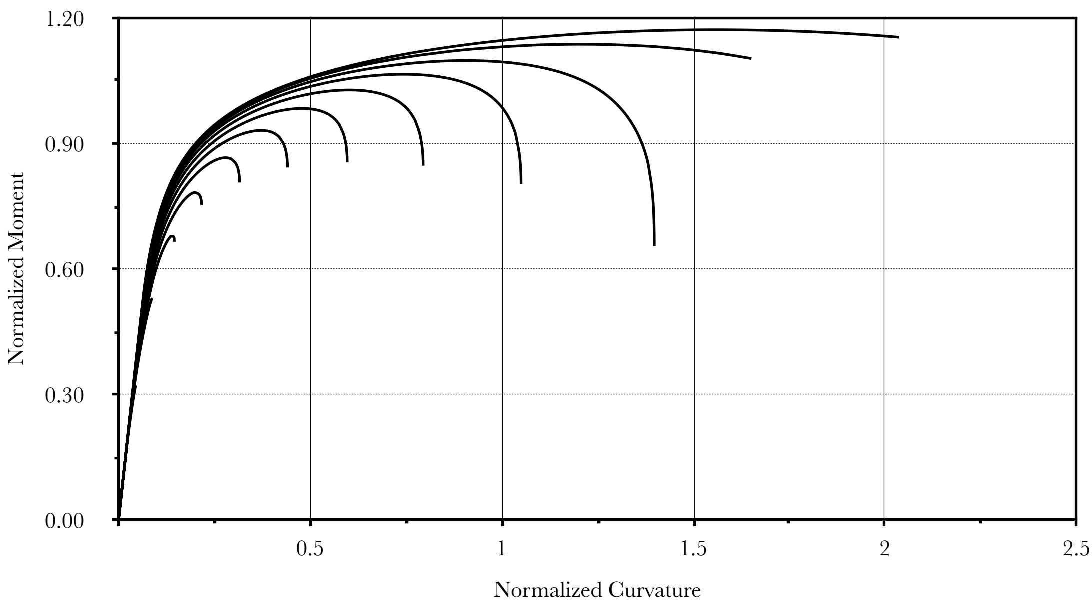

Fig. 5.7 Normalized moment–curvature responses of a ring under bending, for increasing levels of constant external pressure ($D_m/t = 33.94$, $\Delta o = 0.04\,\%$)

E., Madhavan, R., & Babcock, C. [5], except for a slight deviation in the pure bending case, where initial wrinkling is foremost.

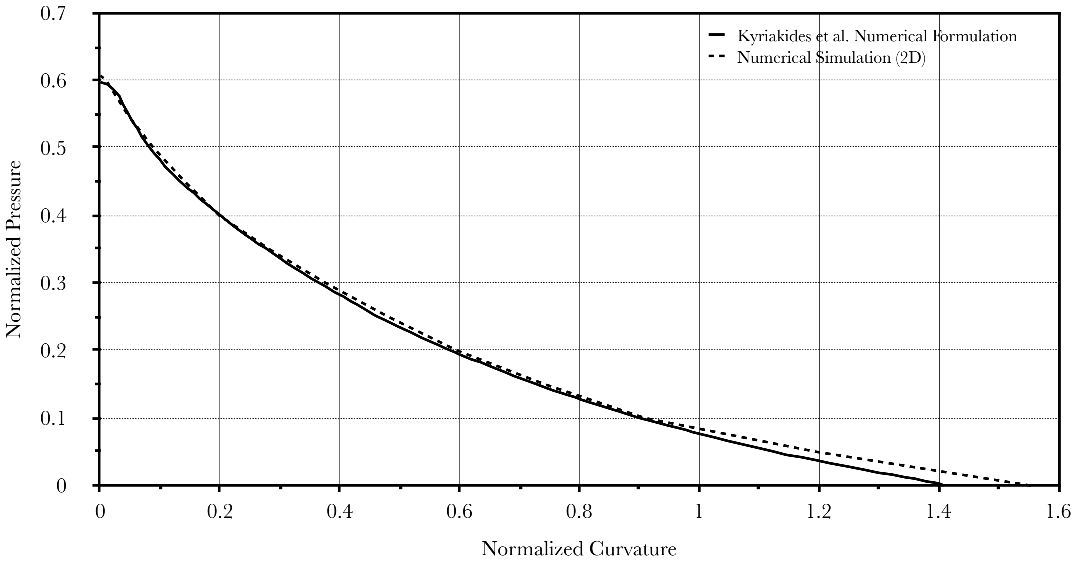

Fig. 5.8 Normalized pressure–curvature pairs of a ring under bending, for increasing levels of constant external pressure in comparison with Kyriakides' numerical formulation ($D_m/t = 33.94$, $\Delta o = 0.04\,\%$)

5.5 Pipe Candidate for Deepwater Application

A tube of $D_m/t = 18.35$ and $D_m = 385.4\,\text{mm}\,(t = 21\,\text{mm})$ is examined in this paragraph. This pipe is considered a suitable candidate for deep water installation at 2 km depth due to its low D_m/t ratio and its suitability can be verified by the Limit State Design methodology, introduced in API 1111 [14]. External pressure is the design criteria for this pipe

$$f_o\ P_{co} \geq (P_{outer} - P_{inner}) \tag{5.1}$$

where f_o is the collapse factor and is equal to 0.7 for seamless pipes, the collapse pressure is given in equation (2.21) and P_{outer} and P_{inner} are the external and internal pressure of the pipeline during installation, respectively. Since the pipeline is installed empty, $P_{inner} = 0$ and at the desired depth, $P_{outer} = 20.1$ MPa. By substituting in the above equation

$$P_{cr} \geq 35.47\ \text{MPa} \Rightarrow t \geq 16.65\ \text{mm}$$

resulting in a safety factor of $sf = 0.80$, for uncertainties during installation.

Being a thicker tube, it is expected that both two as well as three-dimensional models will produce similar results for zero, or very low, initial wrinkling in the three-dimensional formulation. A three-dimensional model was adapted for this analysis of a tube subjected to combined loading. The material is carbon steel $X65$ with no yield anisotropy. A initial ovality of $\Delta_0 = 0.5\,\%$ and length of $L = 21D_m$ is assumed for the tube as well as an initial wrinkling imperfection of 1 % amplitude. The same mesh configuration as previous combined pressure and bending models is used. A parametric study on the effect of initial wrinkling of the tube is then conducted. Initial wrinkling of 5 % , 10 % and 15 % are introduced into the model. As before, numerical analyses of pure pressure, pure bending and combined bending with 5 % increments of the yield pressure, P_y, as constant external pressure levels are conducted. Only the two extreme cases for initial wrinkling of 1 % and 15 % are shown in **Fig. 5.9** and **Fig. 5.10** respectively.

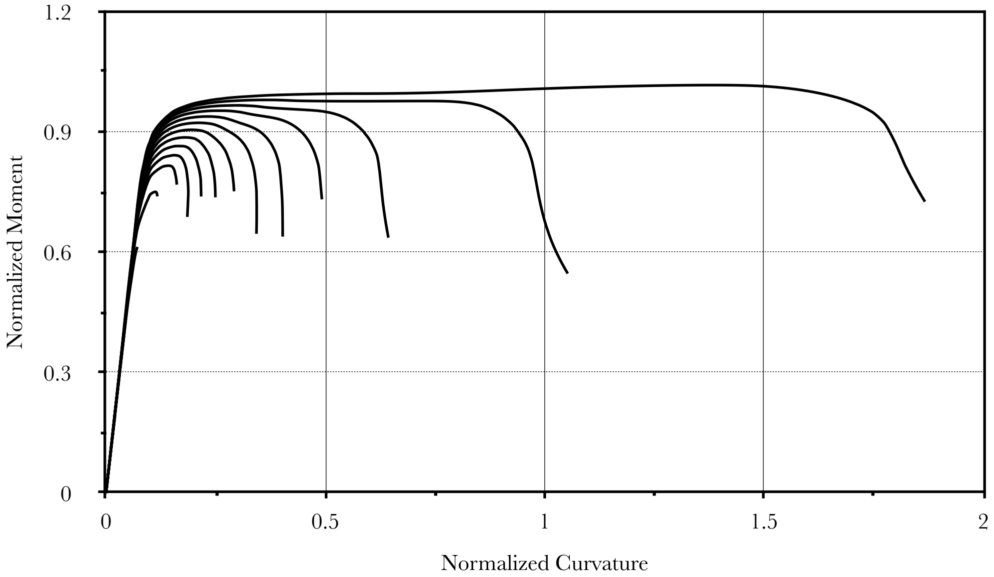

Fig. 5.9 Normalized moment–curvature responses of a three-dimensional pipe with 1 % initial wrinkling under bending, for increasing levels of constant external pressure ($D_m/t = 18.35$, $\Delta o = 0.5\%$, $w_o = 1\%$)

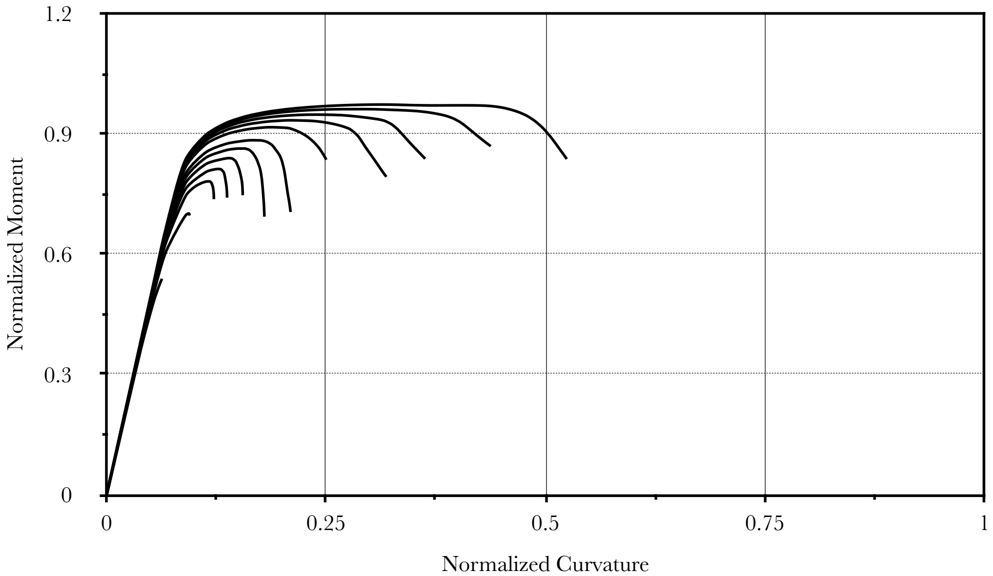

Fig. 5.10 Normalized moment–curvature responses of a three-dimensional pipe with 15 % initial wrinkling under bending, for increasing levels of constant external pressure ($D_m/t = 18.35$, $\Delta o = 0.5\%$, $w_o = 15\%$)

The (κ, P) data pairs are extracted from each simulation and illustrated on a pressure-curvature plot in **Fig. 5.11**. The results show that a larger initial wrinkling imperfection rapidly degrades the stiffness of the tube when subjected to pure bending, however, as the external pressure percentage increases, it is less affected.

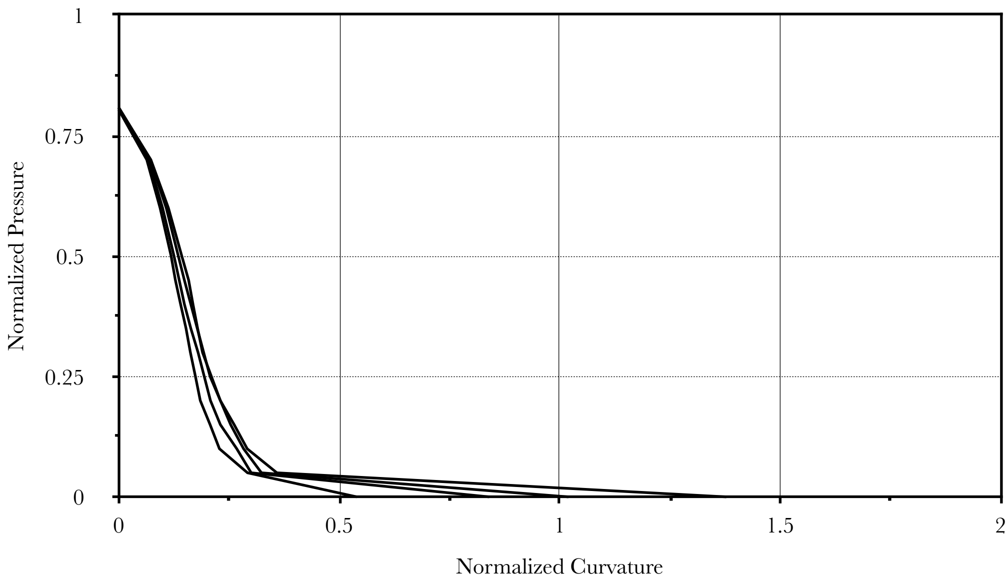

Fig. 5.11 Normalized pressure–curvature pairs of a cylinder with a range of 1% – 15% (right to left) initial wrinkling under bending, for increasing levels of constant external pressure ($D_m/t = 18.35$, $\Delta o = 0.5\%$)

Thicker tubes collapse near the yielding pressure, utilizing the material properties to the maximum capacity, therefore it should be no surprise that altering the material curve can change the tube's response. Considering the original tube ($w_o = 1\%$), two additional materials, both with the same yield stress σ_y but different hardening, are utilized to examine the response of the pipe. A bilinear material is considered first

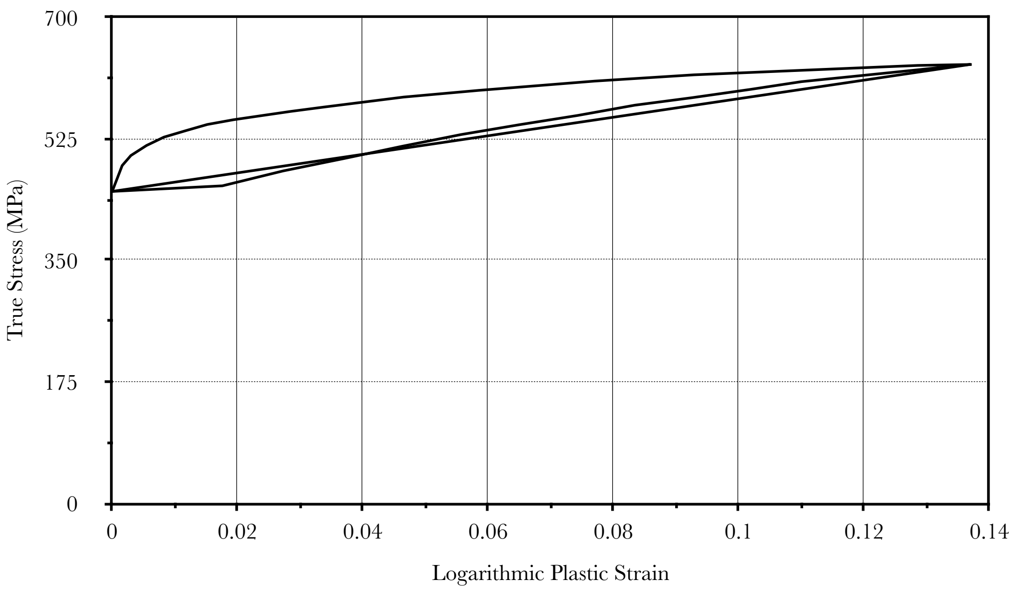

Fig. 5.12 True stress-logarithmic plasticity strain material curves. Top to bottom: Greater hardening, Bilinear, $X65$

where a straight line connects the yield stress and the ultimate stress, which is a simplified way to approximate elastic-plastic behavior. Subsequently, a material exhibiting greater hardening is modeled using a Ramberg-Osgood curve, following the same approach as in previous chapters with $n = 24.9$ and $\sigma_{ro} = 448.44\,\mathrm{MPa}$. The material true stress-logarithmic plasticity strain curve for each case is shown in **Fig. 5.12**. The corresponding $m - \kappa$ (moment-curvature) plots are compared in **Fig. 5.13**. As expected, the influence of the material properties is clearly reflected in the responses, with the greater hardening material withstanding a larger maximum moment.

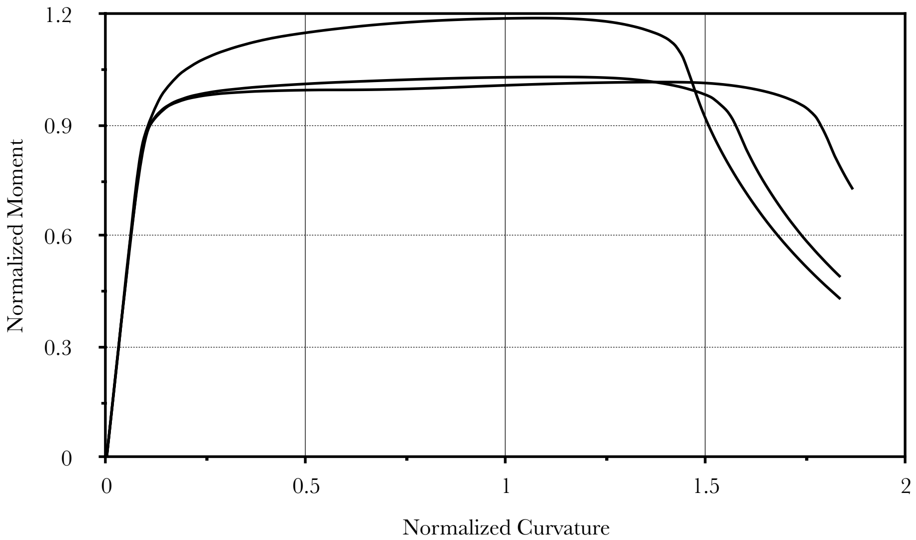

Fig. 5.13 Normalized Moment-Curvature responses. Top to bottom: Greater hardening, $X65$, Bilinear

Chapter 6 – Summary

This thesis investigated the structural behavior of steel pipelines in the overbend and sagbend regions during the S-lay installation method, which are critical due to the combined loading experienced by the pipeline and play a key role in pipeline design, ensuring structural integrity. The behavior of the pipeline has been studied numerically through the general-purpose finite element program ABAQUS/Standard, utilizing both two and three-dimensional models to replicate the loading conditions in these two regions.

The second chapter examined the mechanics of tubes under pure pressure and pure bending. The buckling and the collapse pressure of an elastic ring were formulated, along with the first yield pressure for an inelastic ring. Additionally, the Brazier effect was explained for a tube subjected to bending. This theory provided the foundation for the work that followed.

In the third chapter, tubes under combined loading condition were studied numerically. Initially, the concept of initial ovality was introduced and two as well as three-dimensional models of cylinders under pure pressure, pure bending and combined pressure and bending were created with the purpose of examining their behavior under such loading profiles. Also, the collapse mechanism of inelastic rings was discussed along with Budiansky's analysis on the post-buckling behavior of elastic rings and comparisons between numerical results and analytical solutions were presented for both cases. A key takeaway from this chapter is that any tube under pure pressure can be modeled as a ring, whilst only thicker tubes (intermediate to low D_m/t) can be modeled in two dimensions with high accuracy when subjected to combined bending and pressure. Also, the meshing characteristics developed in this chapter were utilized in every subsequent model.

Chapter 4 focused on the overbend region in the S-lay installation method. Specifically, the experiment conducted by Dyau, J. Y., and Kyriakides, S. [6] of a tube bent over a rigid surface was numerically replicated in two and three dimensions, and the numerical formulations reproduced. The results of the three dimensional replication in a finite element environment overestimated the response measured in the experiment, however, the trend was accurately captured. The results produced by the two dimensional model were in very good agreement.

Chapter 5 examined the sagbend region by numerically replicating the experiment conducted by Kyriakides, S., Corona, E., Madhavan, R., & Babcock, C. [5] of a tube subjected to combined pressure and bending and comparing the results with both the experimental data and prior numerical formulations. The numerical formulation of the experiment seems to underestimate the strength of the tube, although the trend is correctly followed. This could be a byproduct of the real material properties not being adequately captured by the Ramberg-Osgood curve and other unknown variables such as the length that the solid rod extensions were inserted into the tube ends. As for the two-dimensional formulation, it seems to be in very good agreement with the numerical formulation, except for the pure bending case where the ovalization curvature is overestimated, showcasing how in thicker tubes a two-dimensional model suffices for studying combined loading conditions. A case study evaluated the effect of initial wrinkling in a tube and the impact it has to the limit moment and ovalization curvature, finding that a higher percentage significantly hinders the loading capacity of the tube, especially under pure bending. This effect is diminished as external pressure is increased. The effect of varying material hardening paths on the ovalization curvature were also investigated and the influence of the material properties was clearly reflected in the responses.

References

[1] Kyriakides, S., & Corona, E. (2007). Mechanics of Offshore Pipelines: Vol. 1 Buckling and Collapse. Oxford: Elsevier. https://doi.org/10.1016/b978-0-08-046732-0.x5000-4

[2] Karamanos, S. A. (2023). Structural Mechanics and Design of Metal Pipes: A Systematic Approach for Onshore and Offshore Pipelines. Oxford: Elsevier. https://doi.org/10.1016/C2020-0-02505-3

[3] Karamanos, S. A. (2002). «Bending instabilities of elastic tubes». *International Journal of Solids and Structures*, 39 (8), 2059-2085. https://doi.org/10.1016/s0020-7683(02)00085-9

[4] Καραμάνος, Σ.Α. (2003). Σημειώσεις Μαθήματος Μη-Γραμμική Ανάλυση Κατασκευών Ευστάθεια.

[5] Kyriakides, S., Corona, E., Madhavan, R., & Babcock, C. (1989). «Pipe collapse under combined pressure, bending, and tension loads». *Offshore Technology Conference*. https://doi.org/10.4043/6104-ms

[6] Dyau, J. Y., & Kyriakides, S. (1992). «On the Response of Elastic-Plastic Tubes Under Combined Bending and Tension». *Journal of Offshore Mechanics and Arctic Engineering*, *114* (1), 50–62. https://doi.org/10.1115/1.2919952

[7] Murphey, C.E. & Langner, C.G. (1985), «Ultimate Pipe Strength Under Bending, Collapse and Fatigue», *Proceedings of the 4th International Conference on Offshore Mechanics and Arctic Engineering*, 1, 467–477, Dallas, USA

[8] Timoshenko, S. (1933), «Working Stresses for Columns and Thin-Walled Structures», *Journal of Applied Mechanics*, 4, 173-177. https://doi.org/10.1115/1.4012225

[9] Brazier, L. G. (1927). «On the flexure of thin cylindrical shells and other "thin" sections». *Proceedings of the Royal Society of London Series a Containing Papers of a Mathematical and Physical Character*, 116 (773), 104–114. https://doi.org/10.1098/rspa.1927.0125

[10] Palmer, A.C., & Martin, J.H. (1975), «Buckle propagation in submarine pipelines», *Nature*, 254, 46–48. https://doi.org/10.1038/254046a0

[11] Hill, R. (1948), «A theory of the yielding and plastic flow of anisotropic metals», *Proceedings of the Royal Society A,* 193, 281-297. https://doi.org/10.1098/rspa.1948.0045

[12] Karamanos, S.A. & Eleftheriadis, C. (2004), «Collapse of pressurized elastoplastic tubular members under lateral loads», *International Journal of Mechanical Sciences*, 46 (1), 35–56. https://doi.org/10.1016/j.ijmecsci.2004.02.015

[13] Bardi, F., & Kyriakides, S. (2006). «Plastic buckling of circular tubes under axial compression—part I: Experiments». *International Journal of Mechanical Sciences*, *48* (8), 830–841. https://doi.org/10.1016/j.ijmecsci.2006.03.005

[14] American Petroleum Institute (2015). API recommended practice 1111: Design, construction, operation, and maintenance of offshore hydrocarbon pipelines (limit state design). Washington, DC, USA

[15] Budiansky, B. (1974), "Theory of Buckling and Post-Buckling Behavior of Elastic Structures", *Advances in Applied Mechanics*, 14, 1–65. https://doi.org/10.1016/S0065-2156(08)70030-9